

A Guide to Electrocatalyst Stability Using Lab-Scale Alkaline Water Electrolyzers

Raul A. Marquez,[†] Michael Espinosa,[†] Emma Kalokowski,[†] Yoon Jun Son,[‡] Kenta Kawashima,[†]

Thuy Vy Le,[†] Chikaodili E. Chukwuneke,[†] and C. Buddie Mullins^{†,‡,||,⊥,▽,}*

[†] Department of Chemistry, The University of Texas at Austin, Austin, Texas 78712, United States.

[‡] McKetta Department of Chemical Engineering, The University of Texas at Austin, Austin, Texas 78712, United States.

^{||} Texas Materials Institute, The University of Texas at Austin, Austin, Texas 78712, United States.

[⊥] Center for Electrochemistry, The University of Texas at Austin, Austin, Texas 78712, United States.

[▽] H2@UT, The University of Texas at Austin, Austin, Texas 78712, United States.

* Corresponding author: mullins@che.utexas.edu

Number of pages: 64

Number of figures and schemes: 31

Number of tables: 2

Table of Contents

Materials and Reagents	3
Electrode Preparation.....	4
Electrolyzer Materials and Fabrication.....	7
Electrolyzer Assembly	13
Electrolyzer Operation	15
Electrochemical Measurements	17
Best Practices and Troubleshooting Notes	22
Supporting Figures, Tables, and Schemes	31
References.....	63

Materials and Reagents

All the electrolytes were prepared with CO₂-free deionized (DI) water (18.2 MΩ·cm). Deionized water was boiled in a 1 L borosilicate Florence flat-bottom flask to remove CO₂, allowed to cool to room temperature in the sealed flask, and stored in polypropylene bottles wrapped with Parafilm. KOH electrolytes were prepared from reagent-grade potassium hydroxide flakes (Sigma Aldrich, 89.5% according to the certificate of analysis). Water electrolysis tests were performed using unpurified electrolytes unless otherwise indicated. We employed our established purification protocol for experiments with purified 1 M KOH.¹ Nickel(II) nitrate hexahydrate (Thermo Scientific, Puratronic, 99.9985% metal basis) was used in Fe purification. We determined electrolyte concentrations via standard acid-base titration following our guidelines.¹ Primary standard potassium hydrogen phthalate (Thermo Scientific, ACS grade, 99.95 – 100.05%) was used for acid-base titrations. Ni foam (99.99%, 80 - 110 ppi) with a thickness of 1.6 mm was purchased from MTI Co. The thickness of the Ni foam electrodes was reduced to 800 μm using a roller press. Ethanol (Pharmco, 99.5%) and hydrochloric acid (Thermo Scientific, 99.999% metal basis) were used to clean Ni foam substrates before electrode preparation. Ni and NiFe plating baths were prepared from nickel sulfate hexahydrate and iron sulfate heptahydrate salts (Thermo Scientific, ACS grade, 99.95%), with boric acid (Fisher Scientific, ACS grade, >99.5%) as the supporting electrolyte and 3,5-diamino-1,2,4-triazole (DAT, Thermo Scientific, 99.2%) as an additive. The pH was adjusted using sulfuric acid (Supelco, ACS grade, 96.6%). Ammonia gas (Airgas, 99%) was used for nitridation. We used the ZIRFON PERL UTP 500 separator designed specifically for alkaline water electrolysis in all experiments. Nickel gauze (Thermo Scientific, 100 mesh woven from 0.1mm wire) was used as the current collector material.

Electrode Preparation

Ni/NF and NiFe/NF electrodes

Nickel foam pieces measuring $20 \times 30 \times 1.6$ mm were prepared by flattening one-third of each piece with nylon-coated jaw pliers to maintain a $20 \times 20 \times 1.6$ mm square as the electrode's active region ($4 \text{ cm}^2_{\text{geo}}$). The flattened section was then trimmed, leaving only a central strip measuring 5×10 mm to serve as the contact during electrodeposition. Next, the pieces were placed inside 50 mL borosilicate beakers and cleaned sequentially using the following solutions while in an ultrasonic bath for 15 min each: (1) ethanol, (2) 3 M HCl, and (3) DI water.

Ni and NiFe films were deposited galvanostatically using a method adapted from Hoang and Gewirth.² Electrodeposition was performed using a two-electrode configuration, with a Ni foam counter electrode (geometric area: $2 \times 2 \text{ cm}^2$) placed exactly 1 cm opposite the working electrode. Different counter electrodes were used to deposit the varied metal films (Ni or NiFe) to eliminate the risk of cross-contamination. The working electrode was securely fastened with a titanium clip holder and positioned parallel to the counter electrode. A 50 mL glass cell, pre-cleaned with nitric acid, was filled with approximately 15 mL of the plating solution and purged with N₂ gas for 5 min. The plating bath consisted of 0.5 M nickel(II) sulfate, 0.4 M boric acid, and 4 mM DAT. When co-depositing Fe, the solution maintained a total metal concentration of 0.5 M, using a bath with equal parts of 0.25 M iron(II) and 0.25 M nickel(II) sulfate. The pH of the solution was adjusted to ~3 using 1 M sulfuric acid.

Upon cell assembly, the films were deposited at a current density of -4 mA·cm⁻² for 600 s, equivalent to a final deposition charge of 2.4 C·cm⁻². Electrodeposition was conducted without stirring, segmented into six intervals of 100 s each, with resting periods of 10 s to minimize

concentration gradients.² Throughout the process, a steady stream of N₂ gas flowed into the cell's headspace to maintain positive pressure and prevent O₂ from entering.

The current density for deposition was based on the electrochemically active surface area (ECSA) of the Ni foam substrate. We used the C_{dl} method in nonaqueous electrolyte (0.15 M KPF₆ in CH₃CN) to determine the ECSA.³ We used a glass cell separated by a porous glass frit for the working and counter electrodes. A platinum mesh (2.5 × 2.5 cm²) served as the counter electrode, while a silver wire enclosed in a Luggin capillary filled with the same electrolyte was used as the reference electrode. The electrolyte was purged with N₂ gas for 10 min, and a constant flow of N₂ was maintained in the headspace throughout the measurements. Following best practices outlined by Morales and Risch,⁴ cyclic voltammetry scans ranging from 10 to 1000 mV·s⁻¹ were conducted around ±200 mV of the open circuit potential (OCP); the current interruption method was used for *iR* compensation, and the current sensitivity was set to 25% higher than the maximum current at each scan rate. Cathodic and anodic currents were plotted against the scan rate, and an allometric function ($y = bv^\alpha$) was fitted to derive the C_{dl} value from constant *b* (**Figure S1**). Based on a specific capacitance of 11 μF·cm⁻² in nonaqueous media,³ we estimated a roughness factor of ~9.89 for the Ni foam, thus the ECSA was ~39.6 cm².

Ni₃N/NF electrodes

Following our previous method, a nickel nitride catalyst layer was grown on the Ni foam substrate. Nickel foam pieces measuring 20 × 20 × 1.6 mm (4 cm²_{geo}) were cleaned in ethanol and DI water in an ultrasonic bath for 10 min each. The Ni foam pieces were dried under vacuum at 60 °C overnight and then oxidized in air within a box-type furnace at 350 °C for 2 h, with a heating ramp of 10 °C·min⁻¹. Next, the NiO/Ni foam precursor was placed into an alumina boat located in the center of a horizontal tube furnace and subjected to nitridation at 450 °C for 4 h at

a heating ramp of $10\text{ }^{\circ}\text{C}\cdot\text{min}^{-1}$ under NH_3 flow (flowrate: $120\text{ cm}^3\cdot\text{min}^{-1}$). After nitridation, the electrodes were allowed to cool naturally to room temperature.

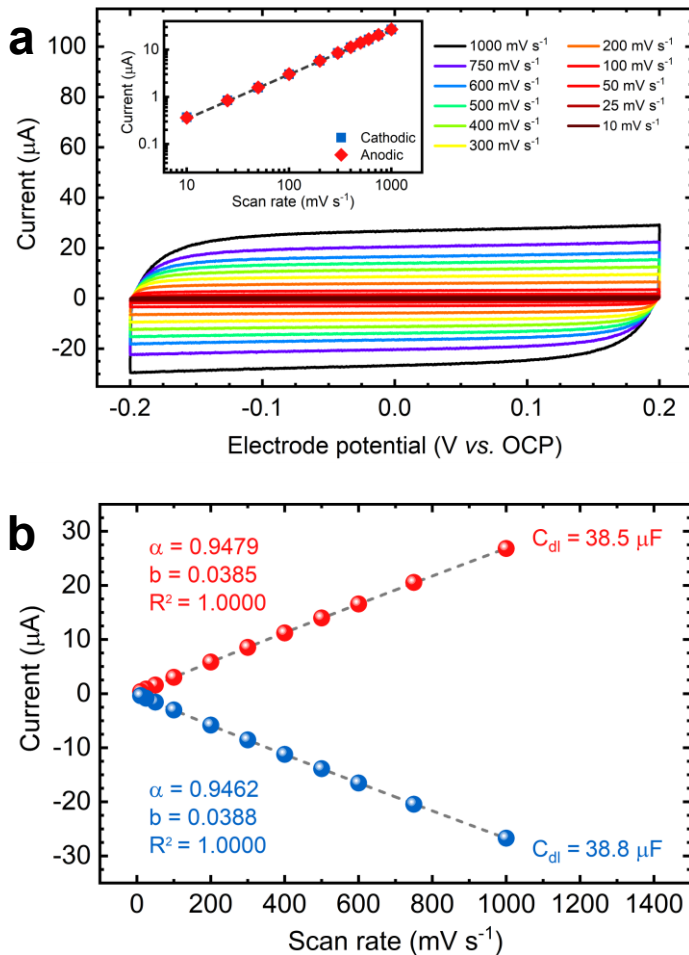


Figure S1. Estimation of the ECSA of the Ni foam substrate in CH_3CN with 0.15 M KPF_6 electrolyte: (a) CV scans near the open circuit potential and (b) anodic (red) and cathodic (blue) currents (at 0 V vs. OCP) as a function of the scan rate.

Electrolyzer Materials and Fabrication

Electrolyzer flow plates

We designed and constructed a standard flow plate with a circular pattern, serving as a flow field to distribute the electrolyte through the plate efficiently. Additionally, we incorporated two cylindrical barbed fittings for connecting the inlet and outlet silicone tubing lines. These components were designed using the SolidWorks 3D CAD software, and the .stl files for each part are provided in a supplementary .zip file. We hope that by providing these files, other researchers can utilize or adapt our design as needed.

The flow plates were machined from acrylic plates (thickness: 1 in) using CNC machining. For simplicity in manufacturing, we machined the barbed fittings separately and glued them to the main flow plate using acrylic plastic cement (Weld-On Adhesives). The integrity of the assembly was verified by testing for leakages at 4 psi air pressure after an overnight drying period. Additionally, we secured a stainless-steel nut in the hexagonal hole to keep the current collector mesh in place. **Figure S2** shows photographs of the assembled flow plates.

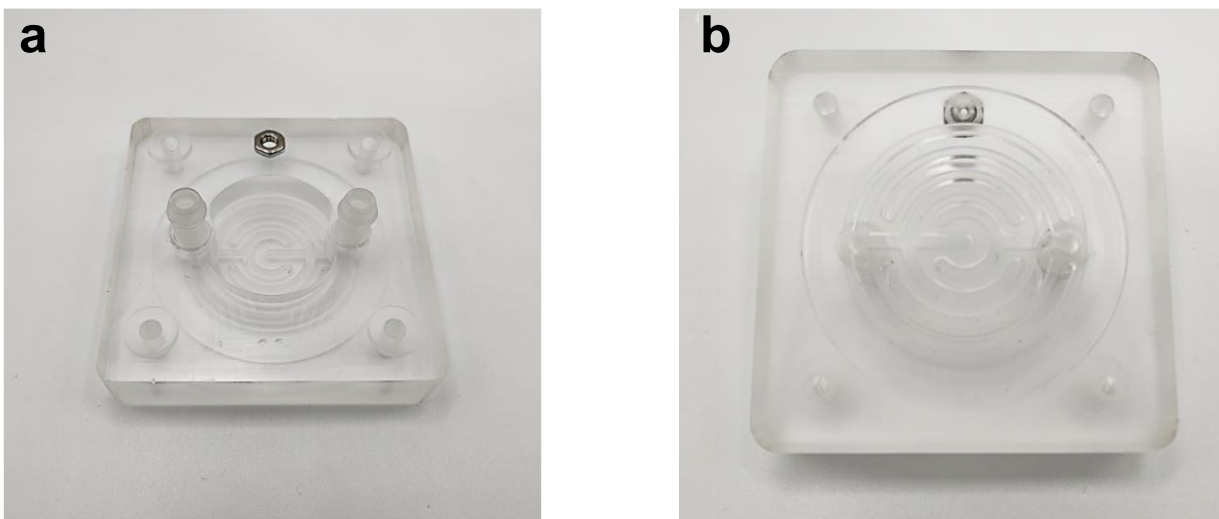


Figure S2. Photographs of the acrylic flow plates: (a) external view of the flow plate and (b) close-up view highlighting the flow pattern on the interior side of the plate.

We chose acrylic for its straightforward manufacturing process and ease of use compared to other specialty plastics. Our team has also experimented with fabricating similar designs from polytetrafluoroethylene (PTFE) plates. Furthermore, we have demonstrated the feasibility of producing these flow cells through 3D printing, offering rapid prototyping and enhanced customization options.⁵

Although we make this design publicly available for adaptation, we encourage its adoption as a standard to facilitate comparability across experiments. Researchers should note that alterations in the size and geometry of this cell design might affect its mass transfer characteristics and hydrodynamics. We advise those who wish to modify this design to adhere to our guidelines for characterizing the mass transfer and hydrodynamics of electrochemical flow cells to ensure proper scaling.⁵

Gasket fabrication

We fabricated circular gaskets from polydimethylsiloxane (PDMS), a transparent elastomer known for its high chemical resistance and inertness, previously used by our group as an electrode coating.¹ We utilized the commercial SYLGARD 184 Silicone Elastomer Kit (Dow). The PDMS gaskets were prepared as follows (see **Figure S3** as reference):

1. We prepared the PDMS liquid by thoroughly mixing the curing elastomer base with the curing agent in a 10:1 ratio for 10 min using a PTFE rod. This mixture was degassed in a vacuum oven for approximately 5 min until all visible bubbles were eliminated.
2. We used the flat ring carved into the flow plate as the gasket mold. We poured the liquid PDMS mixture into this ring and let it settle uniformly. The final gasket thickness depends on the amount of PDMS used; we suggest matching the ring's depth of 500 μm .

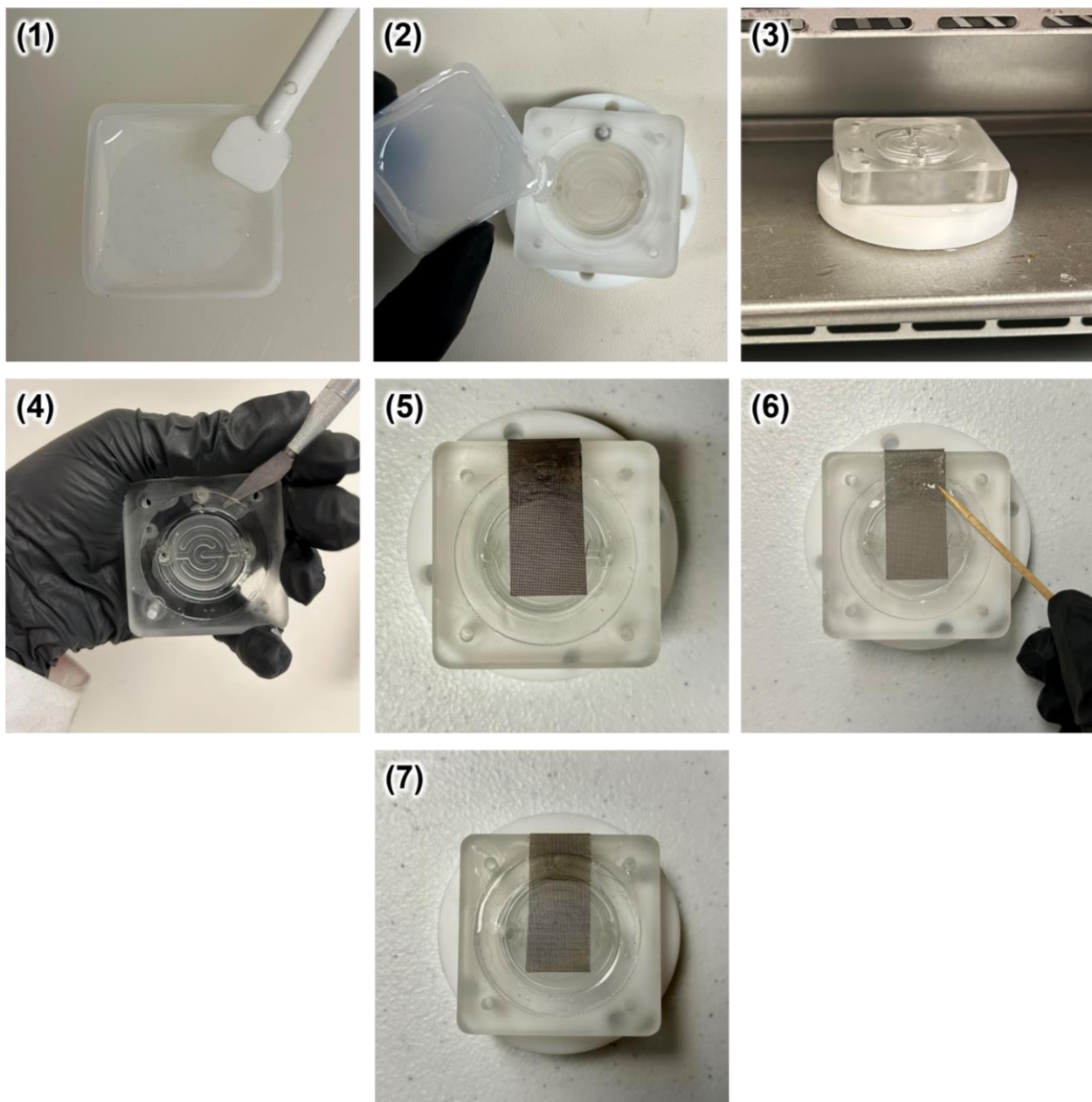


Figure S3. Photographs illustrating the procedure for preparing the PDMS gasket, with each image corresponding to the step-by-step process detailed in the text.

3. The flow plate, supported horizontally on a PTFE holder, was placed on a metallic tray. We cured the PDMS gasket in a small oven at 150 °C for 10 min, adhering to the manufacturer's guidelines. Ensuring the flow plate's horizontal position is crucial for achieving uniform gasket thickness.
4. After curing, the gasket was carefully detached from the mold using a blade.

5. A second PDMS gasket was created following steps 2 and 3 but was not removed from the flow plate this time. Following its curing, we positioned the current collector mesh over it.
6. Next, we evenly spread a small volume of PDMS liquid over the second gasket, still on the flow plate with the current collector in place, and waited 5 min for the PDMS to distribute evenly over the ring.
7. Finally, we placed the first PDMS gasket atop the second and adhered them using the freshly applied PDMS. This assembly was then cured in the oven for an additional 10 min at the same temperature.

As shown in **Figure S4**, the current collector mesh is positioned between the two PDMS gaskets. These gaskets are bonded using the PDMS mixture applied in step 6. By distributing PDMS over the mesh area that overlaps with the gasket ring, the mesh is fully integrated within the two gaskets. If necessary, more PDMS can be added to correct the gasket's thickness. Note that the thickness of the upper gasket layered over the current collector mesh ultimately determines the thickness of the electrode in the final assembly. Thus, this design is compatible with other porous electrode geometries, such as felts or stacked meshes.

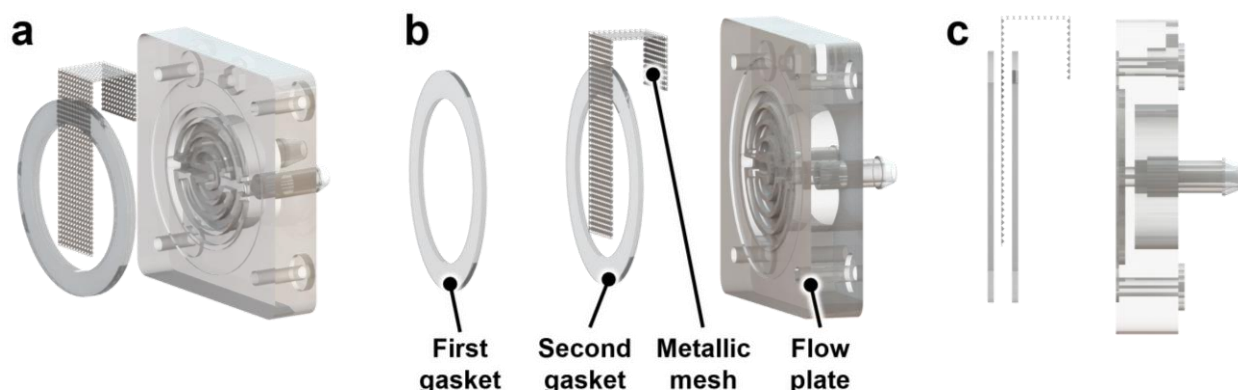


Figure S4. 3D renderings showing the final look of the PDMS gaskets encompassing the current collector mesh: (a) mesh-gasket assembly separated from the flow plate, (b) exploded view of the gasket assembly and (c) side view of the gasket assembly.

Current collectors

We employed metallic meshes as current collectors, integrating them into the gasket seal to simplify the assembly, sealing, and manufacturing processes. Specifically, we used nickel gauze (100 mesh, woven from 0.1 mm wire) to create 2×5 cm strips. These strips were folded to align with the dimensions of the electrolyzer flow plate, as depicted in **Figure S4**. On the strip portion facing outward on the flow plate (see **Figure S2**), we punched a hole approximately 3 mm in diameter. This allowed for the insertion of a M3 stainless steel bolt (4 mm in length) to secure the current collector strip in position. We produced multiple gaskets with an embedded current collector tailored for each experimental scenario to prevent cross-contamination.

Note that alternative metallic gauzes can be used depending on the research requirements. While nickel gauze is preferred to avoid iron impurities and reduce contact resistance issues with Ni-based electrodes, we have also constructed electrolyzers using stainless steel gauze (type 316, 100 mesh woven from 0.11 mm wire) from the same manufacturer. Stainless steel, being more cost-effective, is a viable option in studies where Fe impurities are not a critical concern and where more realistic environmental conditions are simulated. While Ti metallic gauzes are compatible with our design, we advise authors to exercise caution. The formation of an insulating oxide layer on the current collector under alkaline conditions can cause inadequate contact at the electrode/collector interface, leading to increased contact impedance.⁶

Separator

We utilized the commercial ZIRFON PERL UTP 500 separator from Agfa as a standard membrane for alkaline water electrolysis. Each separator was meticulously cut from an A4 sheet using a precision blade on a plastic cutting board. We cut the separators into discs with a

diameter of 34 mm using a plastic mold for consistent sizing. To prepare the separators for use, we followed a conditioning process in an alkaline electrolyte. Following the manufacturer's instructions, we immersed the cut separator pieces in 6 M KOH electrolyte for at least 12 h. This immersion took place in an air-tight plastic container. Before assembling the electrolyzer, a separator piece was carefully retrieved from the electrolyte using plastic tweezers. We then gently removed any excess electrolyte from the separator before assembly.

Additional components

Small copper plates ($10 \times 20 \times 0.675$ mm) were securely attached to the current collector hole on the external side of the flow plate for power connection. This setup facilitated the connection of multiple alligator clips. For the assembly of the electrolyzer, we employed four M3 bolts made of type 316 stainless steel, each 30 mm in length, along with corresponding nuts and washers. The bolts were precisely tightened at 0.3 N·m using a low-range (0.1 – 6 N·m) torque wrench. The flow plates were labeled to ensure accurate identification during experiments, indicating the specific electrode used.

Electrolyzer Assembly

The assembly of the electrolyzer, detailed in **Figure S5**, followed a precise sequential process. Initially, we positioned the anodic flow plate horizontally, ensuring the gasket-current collector assembly was securely in place. Subsequently, the anode, featuring a geometric area of $4 \text{ cm}^2_{\text{geo}}$, was situated within the inner circumference of the gasket, in direct contact with the current collector mesh. Next, we placed the separator carefully atop the anode, aligning it concentrically with the gasket while avoiding any overlap beyond the gasket's outer circumference. The cathode was then aligned and placed over the separator. To complete the assembly, the cathodic flow plate, equipped with its respective gasket, was positioned over the cathode, with meticulous attention to ensure the electrode was enclosed within the gasket's circumference.

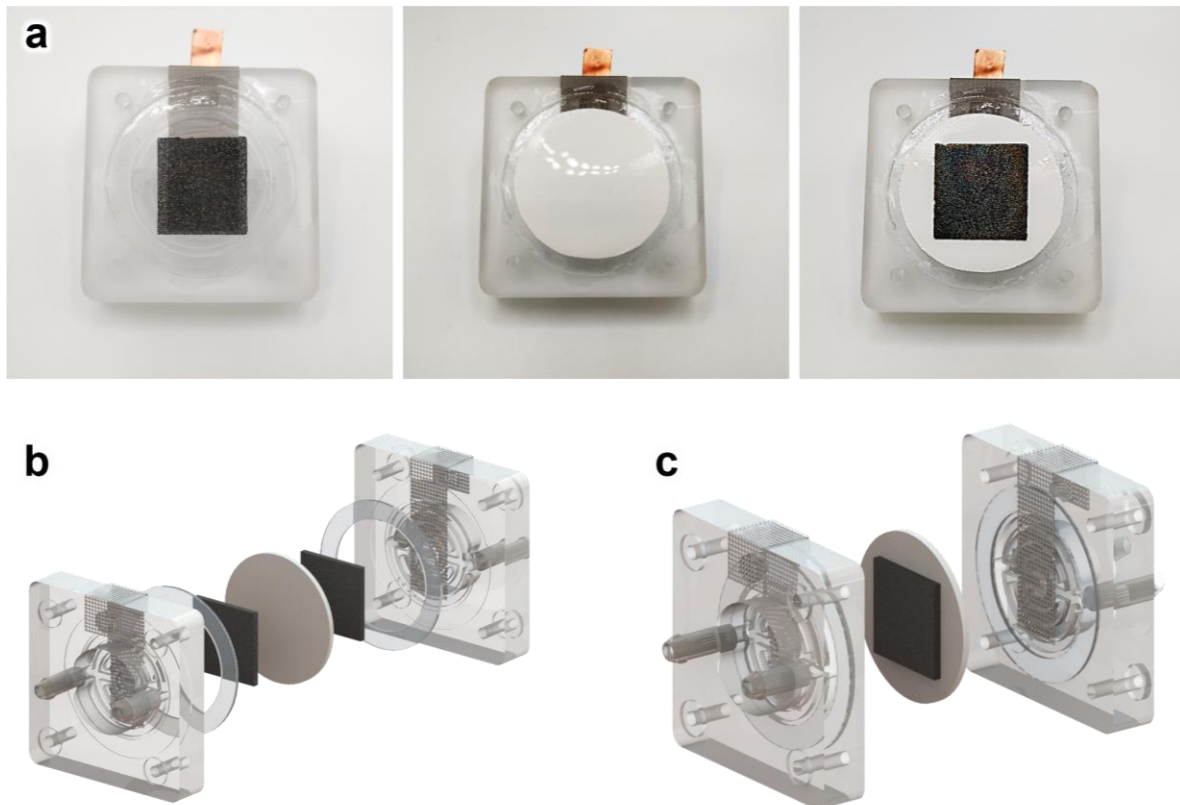


Figure S5. (a) photographs depicting the assembly procedure, starting from placing the anode, then the separator, and then the cathode; 3D renderings depicting the electrolyzer assembly: (b) fully-explored view and (c) close-view of the separator-electrode assembly.

After positioning the electrodes and separator within the flow plates, we inserted four M4 stainless steel bolts through the designated holes near the corner of the flow plates. We then placed the corresponding washers and nuts, initially tightening the nuts by hand. At this stage, it is essential to ensure that the electrodes remain precisely centered and in position. Next, we employed a cross-torquing pattern for further tightening with a torque wrench. This method involved tightening one bolt and then its opposite counterpart. We gradually increased the torque during each round to ensure even tension across all bolts. The bolts were tightened to a final torque of 0.3 N·m for all our experiments. **Figure S6** displays the fully assembled cell, highlighting all components in their respective positions. We also suggest viewing the accompanying video provided with this viewpoint. This video offers a step-by-step visual guide to a typical assembly procedure.

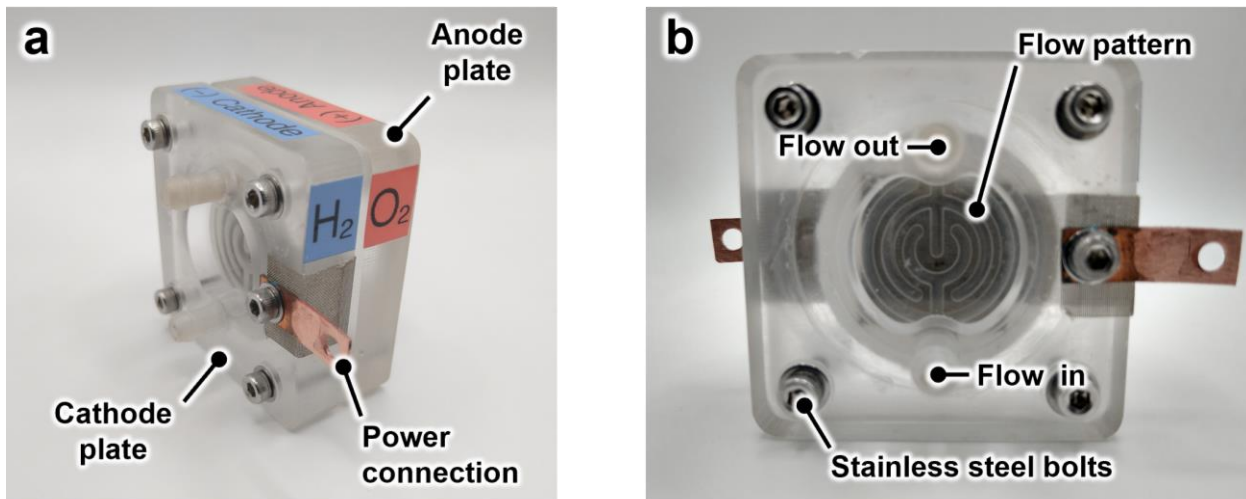


Figure S6. Photographs depicting the custom flow electrolyzer: (a) perspective and (b) side view of the fully assembled electrolyzer.

Electrolyzer Operation

Once fully assembled, the electrolyzer was incorporated into the flow system, as shown in **Figure S7**. We utilized 250 mL Class A glass media bottles as reservoirs for the electrolyte. The bottle caps were modified with two hose barbed fittings (3/16 inch), which served as tubing connectors. We chose high-temperature silicone tubing (Fuel Cell Store, 4 mm ID × 6 mm OD) to ensure durability within the flow circuit. The electrolyte was circulated using peristaltic pumps (KAMOER) equipped with Norprene chemical tubing (3.2 mm ID × 6.4 mm OD), adjusting flow rates between 50 and 200 mL·min⁻¹. We placed the reservoirs in a digital thermostatic water bath (JOANLAB, 6 L) to maintain the electrolyte at a controlled temperature during tests. We monitored the temperature using glass thermometers and stainless-steel thermocouples to ensure precision. Flow rates for both catholyte and anolyte streams were tracked using a liquid flow controller linked to Hall sensor-equipped flow meters (DIGITEN, Model DFC15). The silicone tubing was carefully connected to the electrolyzer's barbed fittings according to the flow scheme shown in **Figure S7a**.

We utilized fresh electrolytes for each electrochemical test. The KOH electrolyte was prepared using volumetric flasks made of polypropylene, in line with our previous guidelines.¹ We degassed the electrolytes with high-purity N₂ for 30 min before measurements using a plastic bubbler. We then circulated the electrolytes through the system and into the electrolyzer to remove any trapped air within the porous foam electrodes until the system reached the targeted flow rate and temperature. Electrochemical tests were conducted in a two-electrode setup. The counter electrode (CE) and reference electrode (RE) alligator clips were connected to the cathode terminal, while the working electrode (WE) was connected to the anode terminal (see **Figure S7b**). Note: we spiked the KOH electrolyte with a fixed and soluble amount of iron nitrate (~1.4

ppm, < 25 μM) to keep iron concentration constant only when testing the stability of the NiFe anode, as recommended by de Groot.^{7,8} All the remaining electrodes were tested in unpurified KOH electrolyte, which contained around 60 ppb of Fe.¹

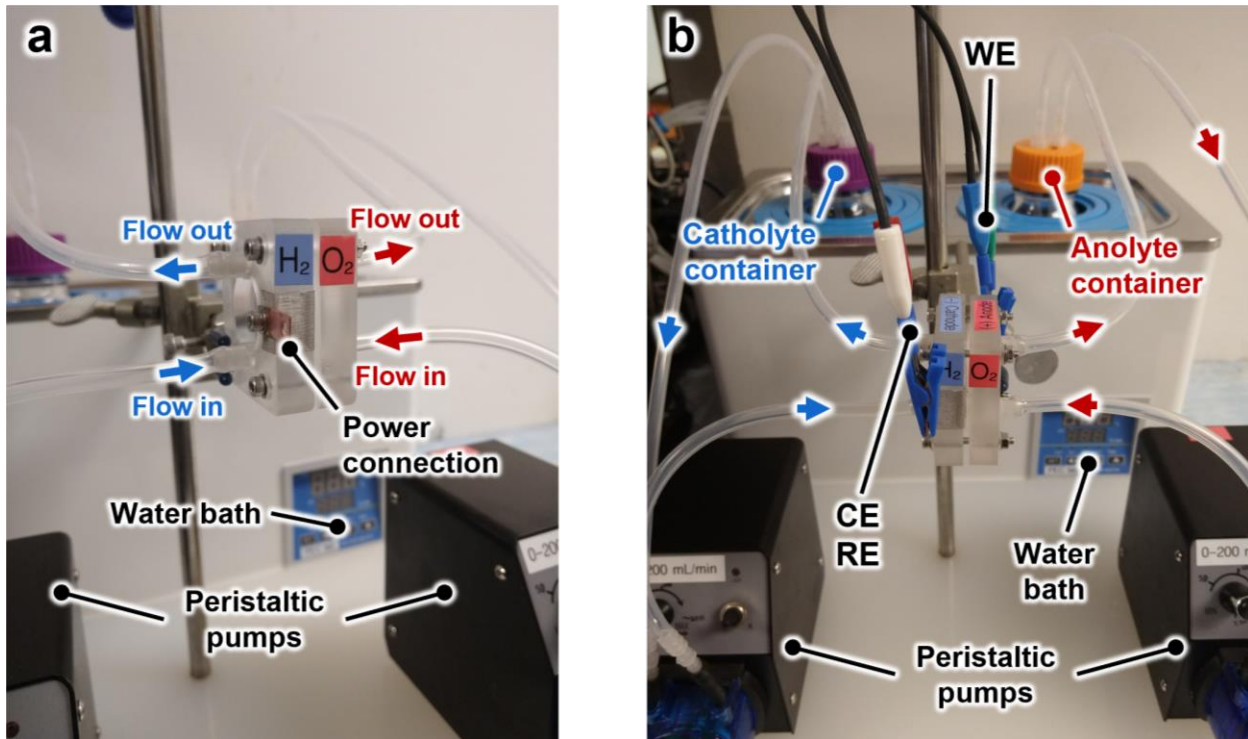


Figure S7. Photographs of the electrolyzer integrated into the flow system: (a) perspective view and (d) side view of the fully operational system.

Electrochemical Measurements

Please refer to **Schemes S1** and **S2** at the end of this document to see a graphical representation of the procedural workflows employed for the electrochemical measurements in this study. The sections that follow provide an in-depth explanation of these workflows.

Electrolyzer startup and conditioning

Electrochemical measurements were conducted using a Gamry Reference 620 potentiostat/galvanostat. The open circuit potential (OCP) was measured during electrolyzer startup, which lasted about two hours on average. After achieving a stable OCP (typically between 0 and -0.1 V, ± 5 mV variation) and reaching the set temperature and flow rates, we conducted electrochemical conditioning via chronopotentiometry for 24 h. Here, a steady current of 60 mA (corresponding to a current density of $15 \text{ mA} \cdot \text{cm}^{-2}$ based on a $4 \text{ cm}^2_{\text{geo}}$ geometric electrode area) was applied while closely observing cell voltage until it stabilized and ensured consistent operating conditions.

Initial performance assessment

Once the electrolyzer was conditioned and the electrodes transformed into the active electrocatalytic phase, the electrolyzer performance was examined before conducting stability tests. Potentiostatic electrochemical impedance spectroscopy (EIS) was utilized to measure the high-frequency resistance (HFR), which reflects the combined ion conduction resistance, R_{ion} , of the electrolyte and separator, and the electronic resistance, R_{el} , which comprises the resistance of the electrocatalytic film and the contact resistances between the electrode, current collector, and electrolyzer terminals:⁹

$$\text{HFR} = R_{\text{ion}} + R_{\text{el}} \quad (1)$$

Potentiostatic EIS measurements were conducted at 0 V and an AC voltage amplitude of 10 mV over a frequency range of 10^5 to 10 Hz.¹⁰ The HFR was obtained from the high-frequency intercept of the Nyquist plot with the real axis.¹¹ Typical HFR values were ~ 250 m Ω for tests at 20 °C in 1 M KOH and ~ 100 m Ω for tests at 50 °C in 6 M KOH.

Next, we recorded complete Nyquist plots by performing galvanostatic EIS tests at the preconditioning current of 60 mA, with a current amplitude of 10 mA over a frequency range of 10^5 to 0.1 Hz.¹⁰ This measurement was repeated three times to ensure reliability. Next, we conducted multistep chronopotentiometry runs to construct full-cell polarization curves. For each step, a constant current was applied for 600 s, immediately followed by galvanostatic EIS at the same current (AC amplitude: 10 mA, frequency range: 10^5 to 10 Hz). The initial current step was set at 4 mA, after which we used the Gamry Sequence Wizard to systematically increment the current using sequence loops. The first loop comprised steps from 8 to 32 mA in 8 mA increments, while the subsequent loop ranged from 40 to 600 mA in 40 mA increments (for example, see **Figure S8b**).

We derived average cell voltages from the final 60 seconds of each step to construct the polarization curves. We determined the HFR for each step to calculate the *iR*-corrected potential, $E_{iR\text{-free}}$, for each corresponding cell voltage, E_{cell} , based on the following equation:¹¹

$$E_{iR\text{-free}} = E_{\text{cell}} - i \cdot \text{HFR} \quad (2)$$

where i is the current applied at each step. The polarization curves and their respective HFR values presented in this study are averaged from three separate experimental runs to ensure reproducibility.

Tafel analysis of iR -free polarization curves was conducted to examine the kinetics of the water-splitting reactions. The Tafel slope was determined by plotting the iR -free cell potential ($E_{iR\text{-free}}$) in the y -axis against the logarithm of the current density (j) in the x axis:^{12,13}

$$E_{iR\text{-free}} = b \log j + C \quad (3)$$

where b is the Tafel slope ($\text{V}\cdot\text{dec}^{-1}$) and C is the y -axis intercept. The exchange current density (j_0) can be derived by extrapolating the linear fit to the equilibrium voltage. The linear fitting was conducted in the low current density region below $30 \text{ mA}\cdot\text{cm}^{-2}$.

In a two-electrode setup, the total overpotential at low current densities comes primarily from the activation of the hydrogen and oxygen evolution reactions (HER and OER, respectively). Therefore, the observed Tafel slope is effectively the sum of the two reactions:

$$b = b_{\text{HER}} + b_{\text{OER}} \quad (4)$$

Distinguishing the contribution of each reaction to the Tafel slope is challenging without making certain assumptions.¹² In our study, one electrode (e.g., the cathode) remained constant, while the other (the anode) was varied. Following the methodology of Ju et al.,¹² where the rate of the HER on a NiH_x surface is assumed to be limited by the Heyrovsky step, the theoretical Tafel slope for the HER can be calculated using Eq. 5:

$$b_{\text{HER}} = 4.6 \text{ RT/F} \quad (5)$$

where R is the gas constant ($8.314 \text{ J}\cdot\text{mol}^{-1}\cdot\text{K}^{-1}$), T is the temperature (K), and F is the Faraday constant ($96485 \text{ C}\cdot\text{mol}^{-1}$). For instance, the theoretical value of b_{HER} is $128.1 \text{ m V}\cdot\text{dec}^{-1}$ at 50°C . Thus, we used the theoretical value for b_{HER} at the corresponding temperature and determined b_{OER} by solving Eq. 4 with the experimental value of b . We did not assume the value of b_{OER} as the OER kinetics could be influenced by Fe incorporation.^{1,14}

Electrolyzer stability tests

This study evaluates two electrolyzer stability tests. In the first test, the electrodes undergo a two-stage current cycle for 60 hours of uninterrupted operation. For this test, we utilized a multistep chronopotentiometry run, with an initial current step of 60 mA ($15 \text{ mA}\cdot\text{cm}^{-2}$) for 10 min. Note: this current corresponds to 10% of the maximum current achievable by our potentiostat, 600 mA, which is also the maximum current registered in the polarization curve. Hereafter, we refer to the 60 mA current as "low load." In the subsequent stage, a higher current step of 480 mA ($120 \text{ mA}\cdot\text{cm}^{-2}$, corresponding to 80% of the maximum current and referred to as "high load") is applied for 20 min. In total, each cycle spans 30 min. Following each cycle, we conduct a galvanostatic EIS run at the low load (AC amplitude: 10 mA, frequency range: 10^5 to 0.1 Hz). The experimental sequence is programmed to replicate these cycles 120 times, giving a total chronopotentiometry duration of 60 h plus the time required for EIS measurements.

The second stability test simulates electrode behavior during a shutdown by incorporating a brief OCP step between the high and low current stages. We utilized two chronopotentiometry steps with an OCP period between loads. Each cycle begins with a high load step of 480 mA for 18 min, followed by an OCP run for 2 min, and concludes with a low load step of 60 mA for 10 min. This sequence also gives a total duration of 30 min per cycle. Galvanostatic EIS experiments were also conducted at the end of each cycle (AC amplitude: 10 mA, frequency range: 10^5 to 0.1 Hz). Similarly, cycles are repeated 120 times using a programmable loop in the experimental sequence.

Furthermore, we acquired full Nyquist plots before and after each stability test sequence via galvanostatic EIS at 60 mA and a current amplitude of 10 mA over a 10^5 to 0.1 Hz frequency range.

Final performance assessment

Following the completion of the electrolyzer stability tests, we assessed the electrochemical performance using the identical sequence and conditions as the initial assessment: (1) potentiostatic EIS at 0 V, (2) galvanostatic EIS at 60 mA, and (3) multistep chronopotentiometry divided in two current loops (from 8 to 32 mA and 40 to 600 mA), followed by galvanostatic EIS at each current step. We derived full-cell polarization curves from the multistep chronopotentiometry plots. Then, we applied the HFR values to **Eq. (2)** for constructing iR -corrected polarization curves. Polarization curves and Nyquist plots were used to compare the electrolyzer performance before and after stability tests.

Best Practices and Troubleshooting Notes

Although operating this alkaline water electrolyzer is relatively simple, particular challenges may arise when preparing the components, starting the electrolyzer, acquiring data, and operating it. We provide guidelines and suggestions on improving the measurements and fixing any problems using this device.

Electrodes, electrolyte, and separator

- *Is electrolyte purification necessary?*

While impurities like iron have been shown to affect the electrocatalytic performance,^{1,15,16} the practicality of using completely purified electrolytes in real alkaline electrolysis settings is challenging.^{7,17} Researchers should judiciously decide on the pertinence of Fe-free electrolytes based on the following considerations:

- (a) Use Fe-free electrolytes to support claims of enhanced electrocatalytic performance.

Solution: Removing Fe impurities is crucial when examining electrocatalytic activity, mainly when attributing remarkable performance to "metal-free" materials or metals known for their low catalytic activity. A control experiment with a Fe-free electrolyte is also advisable to confirm that performance trends are not affected by Fe impurities.

- (b) Keep the electrolyte composition constant throughout your measurements.

Solution: Inevitably, some impurities like Fe will be present in commercial settings. Following de Groot's guidance on managing Fe impurities is recommended.⁷ Aim for a consistent electrolyte composition throughout experiments to ensure performance changes are due to the actual variables being tested. Adding a known amount of impurity may be necessary since electrolyte purity varies among suppliers.¹ Preconditioning is critical to ensure stable electrocatalyst and electrolyte compositions are formed before measuring the electrolyzer performance.

- (c) Consider the scope of your study.

Solution: If the study is centered around operational conditions or other properties of the electrocatalysts (like morphology or mechanical stability), it may be more appropriate to use benchmark and well-known electrocatalysts, such as Ni-based materials. Fe will integrate into the electrocatalyst in unpurified KOH during electrochemical conditioning, forming an active NiFe oxyhydroxide phase. Once this phase stabilizes within the electrolyzer, subsequent variations in stability tests can be ascribed to the specific conditions under investigation. Fe inclusion must contribute to forming the electrocatalytic phase before assessing other properties.

- *There is persistent cross-contamination despite electrolyte purification*

Even with standard electrolyte purification practices, contamination from metals or organics can affect reproducibility and electrocatalytic performance. Consider these potential contamination sources:

- (a) Silicone tubing from prior experiments might retain impurities.

Solution: Thoroughly clean the tubing with concentrated nitric acid after experiments. Flushing with deionized water before and after experiments helps eliminate residue. Before sensitive tests, precondition the tubing with the intended electrolyte and discard it. For rigorous experiments, or after using iron and cobalt catalysts or high-temperature conditions, use new tubing to prevent corrosion-related contamination.

- (b) Although mechanical parts of a peristaltic pump never contact the electrolyte, the tubing can also get contaminated or damaged between experiments.

Solution: Routinely replace pump tubing with materials like Norprene, which better withstands chemical exposure and physical stress, reducing the risk of degradation and contamination.

- (c) Residues and impurities may accumulate in electrolyte reservoirs.

Solution: Clean reservoirs with concentrated nitric acid and consider replacing any plastic components if needed. For glass containers used under extreme conditions, such as high temperatures or strong alkaline solutions, opt for replacement to prevent etching.¹ Where applicable, use PTFE containers or other suitable alternatives based on the specific requirements of your experiments.

- (d) The electrolyzer itself might be the source of impurities.

Solution: Ensure flow plates are cleaned with nitric acid and abundantly rinsed with deionized water. Avoid prolonged exposure of plastic components to strong acids or solvents to prevent material degradation.⁵ For specialized operating conditions, use dedicated components, such as PTFE plates for Fe-free or high-temperature applications and inexpensive acrylic plates for visualizing gas evolution or mass cell production.

- *The separator/membrane is not working properly*

High HFR values may suggest problems with the separator's performance. Consider these corrective actions:

- (a) Inadequate conditioning or activation of the separator.

Solution: Confirm that the separator undergoes thorough conditioning for the recommended duration per the manufacturer's guidelines. If issues persist after following these instructions, consult the supplier for further assistance.

(b) Presence of a residual protective film on the membrane.

Solution: Membranes often come with transparent, rigid films or spacers to protect and maintain their shape. Inspect and remove such protective layers before proceeding with the membrane conditioning process.

Electrolyzer setup

- *Importance of the electrochemical conditioning step*

Electrode conditioning is essential as it facilitates critical processes: (1) complete removal of air trapped within the porous foams, (2) electrocatalyst transformation until the most active and stable phase is formed, and (3) complete electrolyte saturation with H₂ (catholyte) and O₂ (anolyte). The conditioning time should be tailored to achieve a stable final response (i.e., steady state).

(a) The conditioning response keeps changing.

Solution: Extend the conditioning time if needed. A 24-hour standard is recommended, but 12 hours may suffice if the response stabilizes. The ideal duration depends on the electrode's size, composition, substrate, and surface area. If instability persists and factors like bubble release are ruled out, the material may be intrinsically unstable, indicating poor catalytic quality.

(b) The electrolyzer reaches a steady response quickly. Can I use a shorter time?

Solution: While shorter times might seem sufficient, a minimum of 12 hours is advised to ensure material and operational stability. Following this standard will also facilitate comparison in the community.

(c) Can I use other techniques, such as chronoamperometry or cyclic voltammetry?

Solution: Our group has shown that the electrochemical conditioning technique strongly influences the final properties and degree of impurity incorporation of electrocatalytic materials.¹⁸ Therefore, employing alternative conditioning techniques may lead to variations in catalytic properties, complicating the comparison of electrocatalytic materials. Our experience suggests that chronopotentiometry is preferable for its ease of control and consistent current application, especially in two-electrode setups. Nonetheless, alternative methods may be advantageous depending on the specific research context. We encourage exploration into diverse conditioning techniques for optimized electrochemical procedures.

- *There is severe hydrogen gas crossover during tests*

Although the zero-gap configuration used in this study is simple and easy to use, it may result in significant hydrogen crossover through the separator.¹⁹ This is particularly important for tests performed at high currents and when gas products need to be quantified.

Solution: Using a finite gap of ~500 µm on the cathode side has proven to significantly mitigate hydrogen crossover and expand the operating capabilities of alkaline electrolyzers.¹⁹ This gap can be achieved by redesigning the flow plates or incorporating a porous plastic mesh that enhances turbulence.⁵

- *Electrolyte crossover between the catholyte and anolyte*

Electrolyte imbalance between the catholyte and anolyte compartments may become apparent after extended operation due to crossover. To mitigate this issue, consider the following:

- (a) Misalignment of the separator.

Solution: Ensure that the separator is aligned when assembling the electrolyzer. The separator should be concentric to the gasket's circumference without extending beyond its outer diameter.

- (b) The separator was damaged before or during testing.

Solution: Inspect the separator for cracks or damage before use. Avoid reusing separators that have dried out after previous experiments. Always condition new separators before each test. Take extra care when cutting to size, avoid damaging the piece once cut, and consider using molds or protective plastic sheets and cutting boards when slicing with a blade.

- (c) Unequal pressure in flow lines.

Solution: Variations in pump flow rates and hydrostatic pressures in the electrolyte containers can gradually lead to electrolyte crossover. If separating catholyte and anolyte solutions is not critical, connect the reservoirs with a balance line to maintain equal volumes (see the electrolyzer setup in Ref. 19). This line will keep the same electrolyte volume and composition. This configuration is unsuitable if the electrolyte composition is analyzed (e.g., corrosion studies).

- *Using stainless steel thermocouples and other accessories in this setup*

Minimizing the use of stainless-steel components is advisable to reduce contamination. However, it is crucial to consider different scenarios:

- (a) Reduce stainless-steel use whenever possible in lab-scale electrocatalysis research

Solution: In our electrolyzer setup and electrolyte reservoirs, we avoided stainless steel components to prevent corrosion-related incidental effects. Glass thermometers were used instead of stainless-steel thermocouples for temperature monitoring in Fe-purified KOH experiments. However, when temperature control was critical, we used thermocouples, which were only immersed intermittently. We recommend limiting the use of stainless steel, particularly in studies evaluating electrocatalytic material performance.

(b) Situations requiring stainless steel

Solution: Stainless steel may be more appropriate in scenarios that simulate real-world applications. For example, stainless steel reservoirs can enhance heating efficiency, stainless steel tubing can create a more robust electrolyte flow system, and metallic components like compression plates can improve the electrolyzer's durability and operating range in terms of temperature and pressure. These considerations are mainly relevant for industrial applications, where electrocatalysis research may not be the top priority. However, such setups might not be readily achievable or cost-effective for researchers aiming to upscale electrocatalytic materials in a lab setting.

Electrolyzer

- *The electrolyte leaks from the gaskets*

Leakage of the electrolyte from the gaskets indicates non-uniform contact between the gaskets and the flow plates. The following issues may lead to electrolyte leaks:

- (a) The electrolyzer was not assembled uniformly.

Solution: Verify that the plates are correctly aligned before tightening the bolts. The separator should be centered and match the gaskets' circumference without overlapping their outer diameter. The electrode should fit within the inner diameter of the gaskets and not be compressed by them.

- (b) The bolts were not properly tightened.

Solution: Employ a sequential tightening strategy, as each bolt affects the tension of others in the set. Adopt a cross-torquing pattern (tighten one bolt, then the opposite one) and apply gradual torque increments in each round until reaching the specified torque, using a torque wrench to ensure uniform bolt tension.

- (c) The flow plates were broken during tightening.

Solution: Excessive tightening can cause cracks or breaks on brittle plastics like acrylic or cheap 3D printing polymers. Be especially careful when tightening the cell, and use small torque wrenches. We recommend assembling with a low torque ($< 1 \text{ N}\cdot\text{m}$) first, then conducting a leak test by running DI water through the system to spot leaks. If leakage occurs, increment the torque and retest. Once a leak-free torque level is found, consistently apply it during experiments. Different torques might affect the electrolyzer's performance and permanently damage the components.

- *Short-circuit of the cell*

A short circuit in the electrolyzer, typically caused by direct electrical contact between the cathode and anode, signifies a complete system failure, leading to an immediate collapse of cell potential during measurements.

(a) External Short Circuit.

Solution: Stop the measurement immediately and switch off the pumps. Inspect for potential external short circuit sources, such as any metal object bridging the negative and positive terminals. Keep the electrolyzer away from metallic accessories like stands, clamps, or wires. Ensure that alligator clips are not in contact and use insulated clips or ring terminals where possible. All wires and cables should be adequately insulated and kept away from metallic surfaces. Regularly inspect the integrity of the potentiostat's cables.

(b) Internal Short Circuit.

Solution: If the issue is not external, the electrodes inside the electrolyzer have likely touched, possibly due to perforation of the separator. Ensure that the bolt torque applied during assembly was not excessive. Use potentiostatic EIS at 0 V to assess the HFR and identify resistance issues. Another approach is to empty one side of the electrolyte and recirculate the other to test for leaks through the separator (e.g., drain the catholyte and circulate the anolyte to check for permeation through the separator). Whenever possible, use new separators, and for operations involving notably high flow rates and pressures, opt for thicker separators.

- *Why not use a reference electrode in this design?*

Incorporating a reference electrode allows precise control and measurement of the potential of only the working electrode (anode or cathode). Although feasible, there are reasons why it may not be ideal for our system.

(a) Absence of Reference Electrodes in Realistic Electrolyzers.

Solution: Integrating a reference electrode into a practical electrolyzer setup is more complex than it appears. Depending on the RE size, significant adaptations to the electrolyzer design might be necessary, compelling each researcher to develop a unique cell design. While this is not inherently negative, we aim to standardize lab-scale electrolyzer geometries and dimensions to facilitate more effective comparisons across research groups. Our design simplifies manufacturing and scaling to more realistic environments. We recommend using the RE configuration shown in Ref. 20 if an RE is completely necessary. The gasket shown in this work can be made of PDMS, following the instructions shown in **Figure S3**.

(b) Three-electrode cells are more suitable for studies of electrocatalytic activity.

Solution: Three-electrode cells are more suited to the catalyst discovery phase, where precise control over the working electrode is critical. However, our design targets the evaluation of electrocatalyst stability under conditions that are closer to real-world applications. This can be seen as a subsequent phase in the scale-up process – testing the longevity and performance of previously identified active materials under practical conditions. In such scenarios, the individual electrode potential is of secondary importance.

Data acquisition and electrochemical measurements

- *The chronopotentiometry steps do not reach a stable cell potential*

This behavior suggests that the electrolyzer is not entirely stable and may be undergoing changes. Possible reasons include:

- (a) In-situ electrode transformations, such as anode oxidation during the OER, can cause the cell potential to rise or fall during testing.

Solution: Extend the preconditioning period to ensure complete transition to the active electrocatalytic phase. Confirm that the current step duration is adequate; we recommend a minimum of 5 min, though this may vary with different materials.

- (b) Significant voltage fluctuation or noise could indicate issues with gas bubbles, especially at high currents or if the electrolyte is not being pumped.

Solution: Increase the electrolyte flow rate to dislodge bubbles. If the electrode substrate's porosity is too low, switching to one with higher porosity can improve gas release.

- (c) Temperature variations can cause cell voltage instability, which becomes more likely to occur at elevated testing temperatures due to more significant temperature gradients with the surroundings.

Solution: Ensure consistent electrolyte temperature control throughout the test. Utilize thermostatic baths with covers to minimize heat dissipation. Consider upgrading to a more precise temperature control system, mainly when high-temperature conditions are essential.

- *Nyquist plots are noisy*

Due to bubble formation, galvanostatic EIS measurements can become significantly noisy at higher DC currents/potentials. Here are some strategies to enhance the quality of your measurements:

- (c) Acquiring full EIS plots.

Solution: Obtain full Nyquist curves at lower currents or cell potentials. As you increase operational conditions, bubble formation intensifies, limiting the system by mass transport and resulting in noisier Nyquist plots. Raising the flow rate might aid in more effective bubble removal. However, EIS measurements will become more complex as the applied current or potential increases.

- (d) Focusing EIS on HFR measurements.

Solution: If your primary goal is to measure the HFR, consider narrowing the frequency range during EIS. For instance, when targeting HFR, we reduce the frequency span from 10^5 to 10 or 100 Hz, avoiding frequencies below 1 Hz. The HFR

typically emerges rapidly before bubble evolution becomes problematic, so Nyquist plots focused on the HFR region will likely be less noisy.

- *Relevance of the potentiostat's compliance current/voltage:*

Potentiostats have built-in current and potential compliance thresholds to protect the instrument during use. Reaching these limits may trigger various responses from the potentiostat.

(e) Difficulty reaching higher currents/potentials.

Solution: Familiarize yourself with your potentiostat's specifications, particularly its compliance limits, to avoid damaging the equipment. Many potentiostats stop the experiment or display a constant line upon reaching these safety thresholds. Some models allow you to set a secondary current/potential limit for improving the sensitivity, separate from the fixed safety compliance limit. For instance, Gamry potentiostats let you adjust each experiment's maximum current or voltage limit. Ensure your user-defined limit exceeds your anticipated maximum current/potential to allow the instrument to function correctly. However, remember that all instruments have inherent limitations, which should be considered in planning your experiments.

(f) Focusing on current density over total current.

Solution: In electrocatalysis, comparing the performance using current density is more informative than total current. Use smaller active areas that require less total current to achieve a specific current density. For example, if your potentiostat's maximum current limit is 500 mA, using a 2 cm^2 electrode allows you to reach up to $250\text{ mA}\cdot\text{cm}^{-2}$. In contrast, a 10 cm^2 electrode would limit you to a maximum current density of only $50\text{ mA}\cdot\text{cm}^{-2}$.

- *Checking the HFR during testing*

Regular measurement of HFR is crucial for tracking changes in the system's ionic and electronic conductivity.

(a) How often do I need to check the HFR?

Solution: We advise measuring the HFR before and after significant alterations to the electrode. This includes electrochemical conditioning steps, the construction of polarization curves, or any adjustments in operating conditions like temperature. Additionally, assessing HFR after stability test cycles is essential to monitor any alterations over extended periods. Regular HFR checks can help pinpoint specific events during long-term testing.

(b) Additional applications of the HFR.

Solution: Beyond its primary use, HFR can identify conductivity issues, potential short circuits, separator deterioration, or temperature fluctuations. EIS should be

considered a fundamental tool for comprehensive electrolyzer characterization, offering valuable insights beyond standard performance metrics.

- *I do not have a potentiostat. Can I use a power supply?*

Depending on the type of power supplies, these can be highly robust and suitable for testing the electrolyzer performance. Consider the following aspects:

- (a) My power supply does not have a software or programmable interface.

Solution: If that is the case, you may need to manually record the average cell potential after applying a particular current step, for example, when constructing polarization curves. Programmable power supplies are worth investing in because sequential cycles can be programmed for stability tests and polarization curve construction.

- (b) Limitations of electrochemical measurements and scope of use.

Solution: Depending on the power supply, different electrochemical techniques, such as EIS, might not be available. This is one of the main limitations of using power supplies instead of potentiostats. However, one could use power supplies if the scope of the study is to examine other aspects of electrocatalytic stability, such as detection of products, ex-situ characterization and post-mortem analysis of the materials after rigorous testing, characterization of electrolyzer's components, etc. As mentioned earlier, this lab-scale electrolyzer system aims to take the next step in electrocatalyst scale-up. Once the main electrocatalytic processes have been understood, researchers need to take electrocatalytic materials to the next step and confirm their pertinence for commercial water electrolysis in more realistic scenarios.

Supporting Figures, Tables, and Schemes

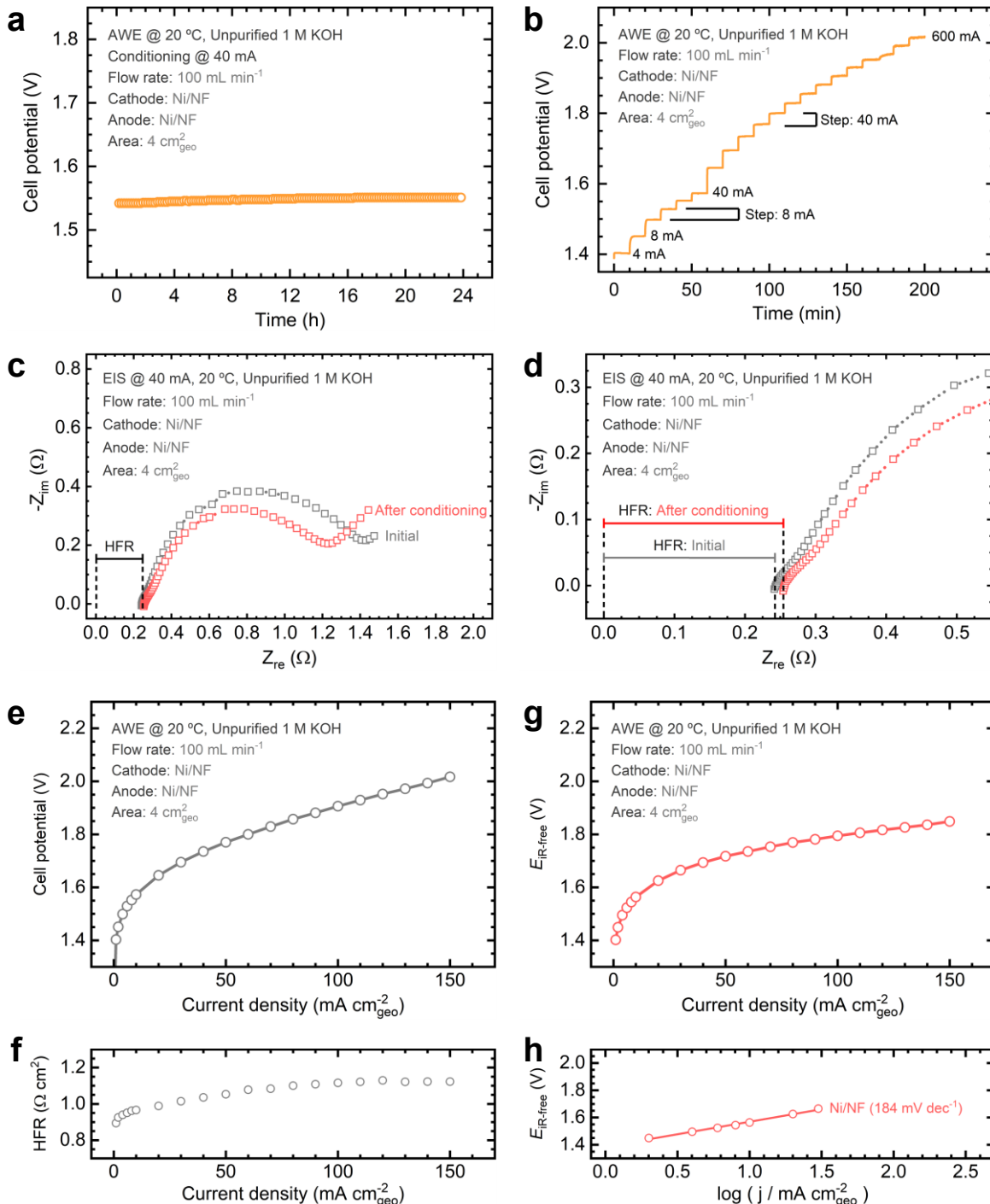


Figure S8. Electrochemical conditioning and initial assessment of the alkaline water electrolyzer operating with Ni/NF electrodes: (a) electrolyzer conditioning at 40 mA for 24 h, (b) multistep chronopotentiometry measurement for constructing polarization curves, (c) full and (d) close-up view of Nyquist plots showing the HFR region, (e) full-cell polarization curve constructed from (b), (f) corresponding HFR values at each current step, (g) *iR*-corrected polarization curve constructed from (e) and (f), and (h) Tafel plot constructed from (g).

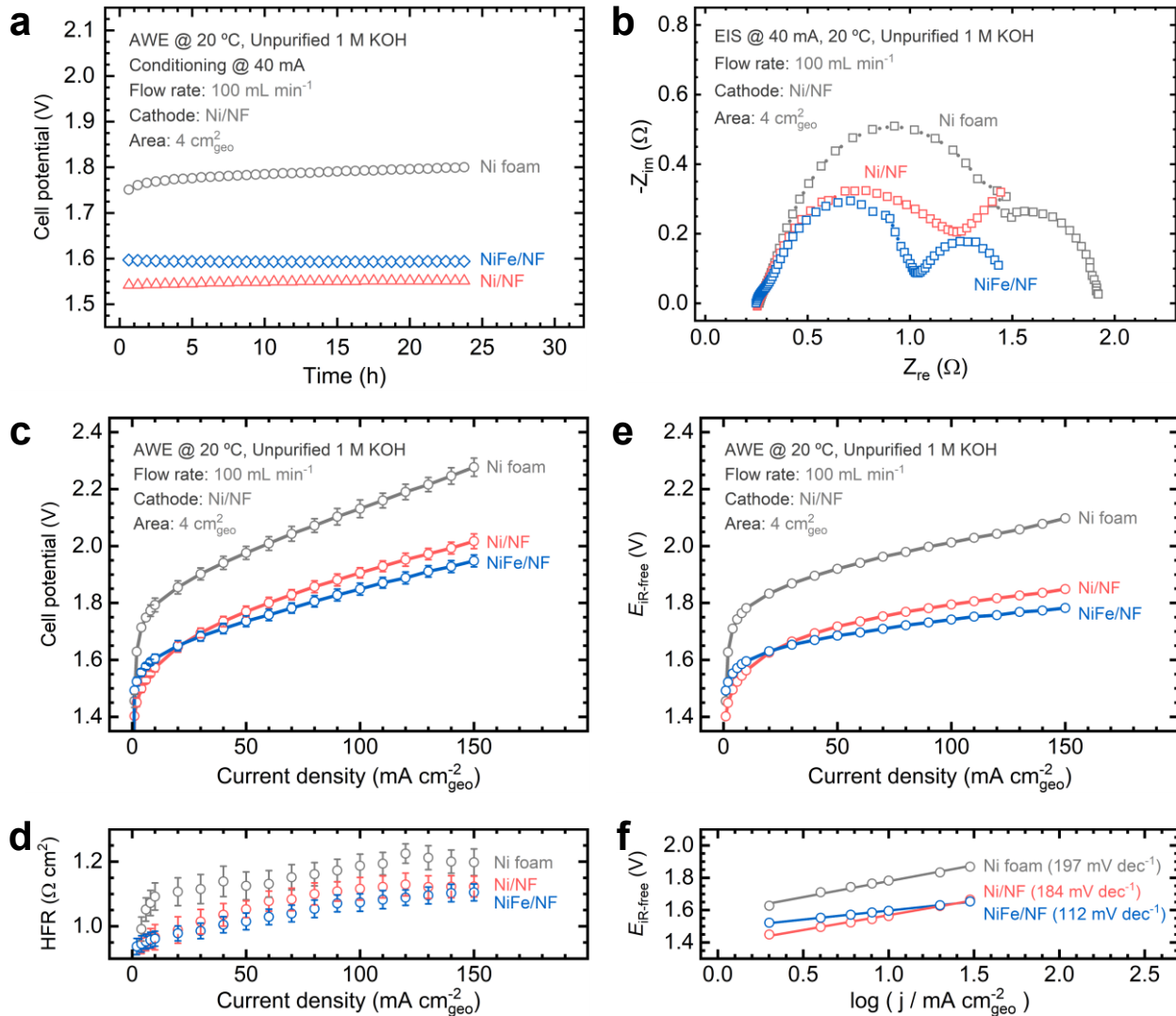


Figure S9. Electrochemical conditioning and initial assessment of the alkaline water electrolyzer operating with different anodes: (a) electrolyzer conditioning at 40 mA for 24 h, (b) full-cell Nyquist plots, (c) full-cell polarization curve, and (d) corresponding HFR values at each current step, (e) *iR*-corrected polarization curve constructed from (c) and (d), and (f) Tafel plots constructed from (e). Experimental conditions: Ni/NF cathode, unpurified 1 M KOH electrolyte at 20 °C, 100 mL·min⁻¹. Uncertainty bars indicate the standard deviation derived from three replicate measurements.

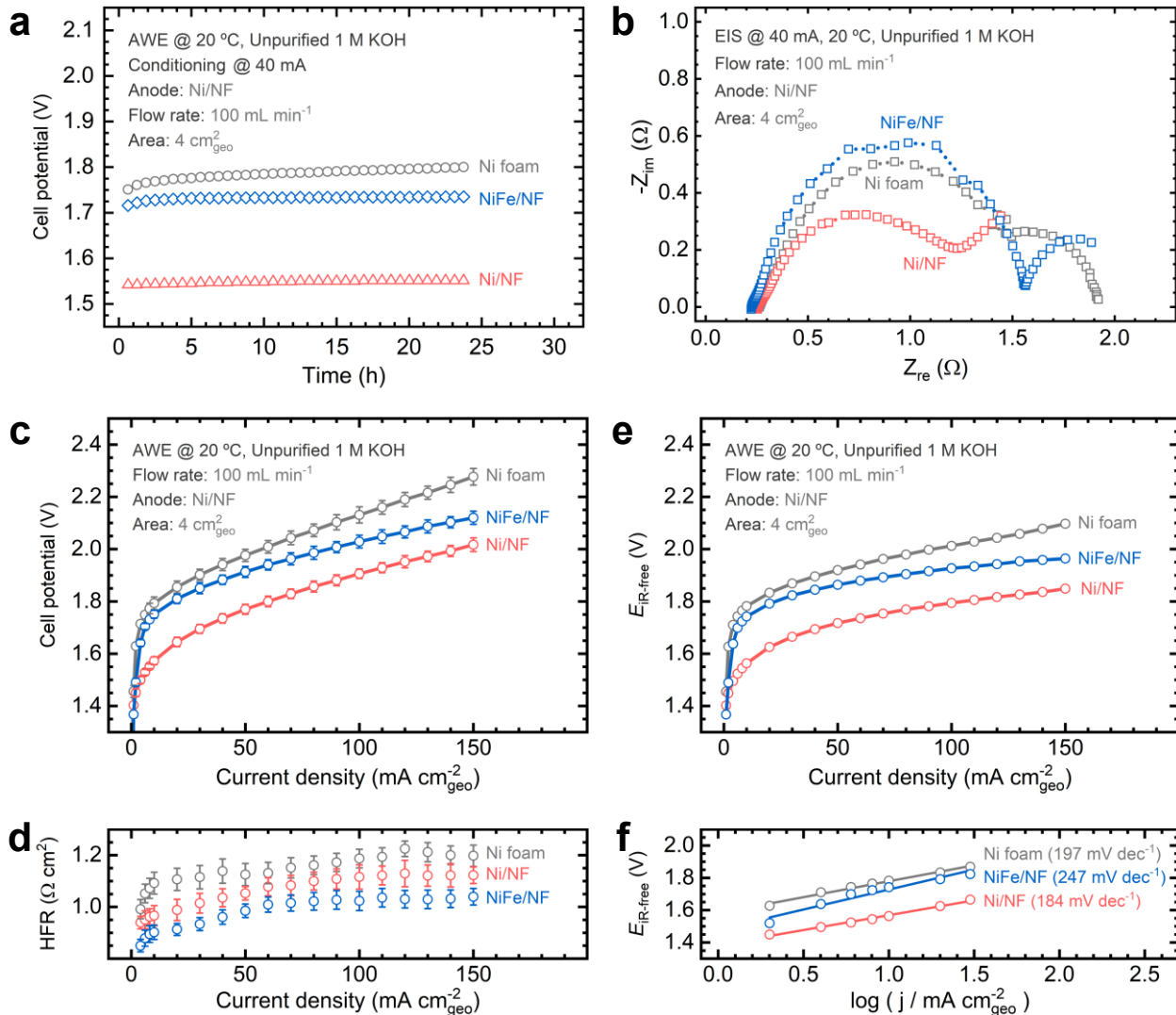


Figure S10. Electrochemical conditioning and initial assessment of the alkaline water electrolyzer operating with different cathodes: (a) electrolyzer conditioning at 40 mA for 24 h, (b) full-cell Nyquist plots, (c) full-cell polarization curve, and (d) corresponding HFR values at each current step, (e) *iR*-corrected polarization curve constructed from (c) and (d), and (f) Tafel plots constructed from (e). Experimental conditions: Ni/NF anode, unpurified 1 M KOH electrolyte at 20 °C, 100 mL·min⁻¹. Uncertainty bars indicate the standard deviation derived from three replicate measurements.

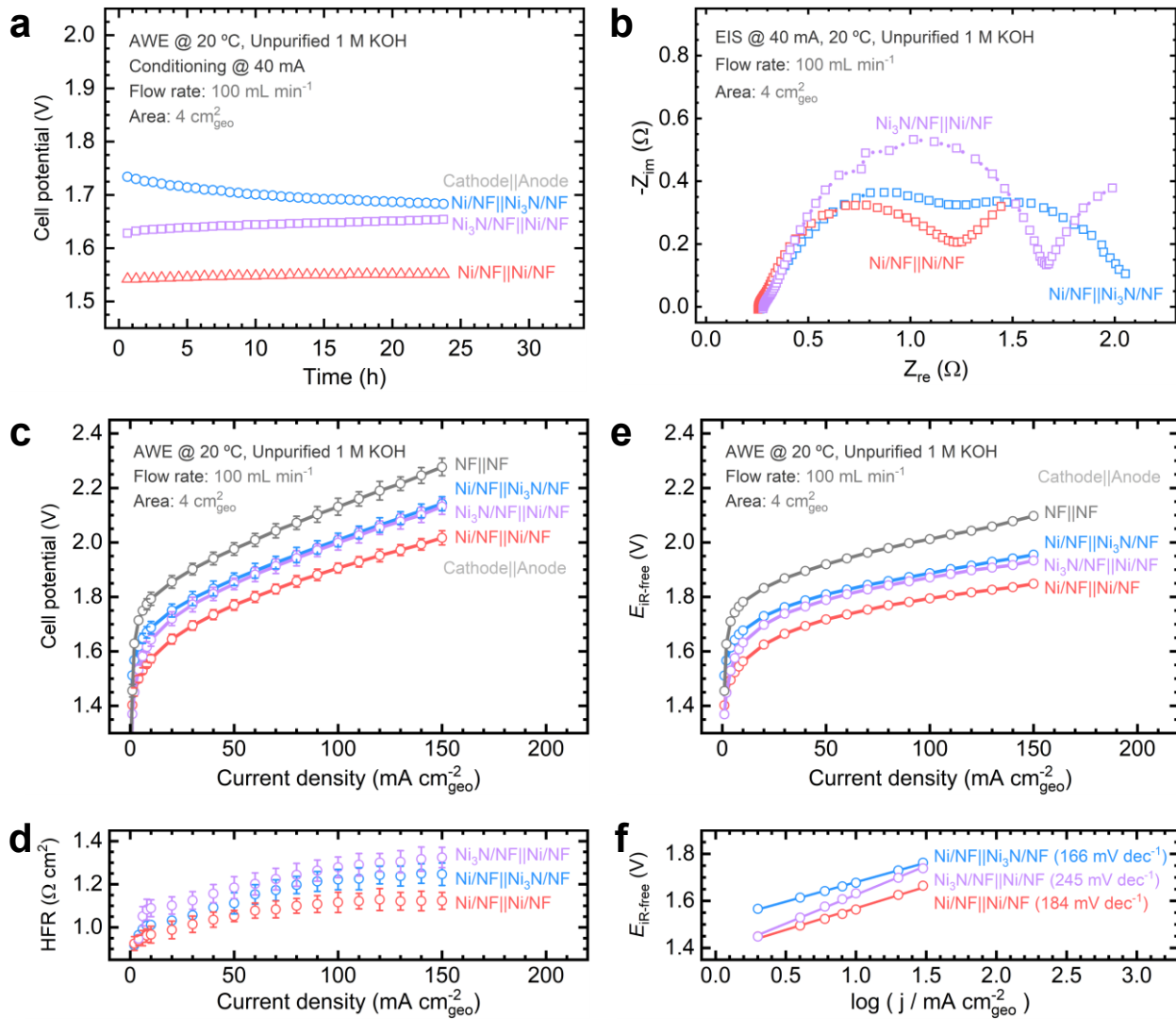


Figure S11. Electrochemical conditioning and initial assessment of the alkaline water electrolyzer operating with different combinations of Ni/NF and Ni₃N/NF electrodes: (a) electrolyzer conditioning at 40 mA for 24 h, (b) full-cell Nyquist plots, (c) full-cell polarization curve and (d) corresponding HFR values at each current step, (e) *iR*-corrected polarization curve constructed from (c) and (d), and (f) Tafel plots constructed from (e). Experimental conditions: unpurified 1 M KOH electrolyte at 20 °C, 100 mL·min⁻¹. Uncertainty bars indicate the standard deviation derived from three replicate measurements.

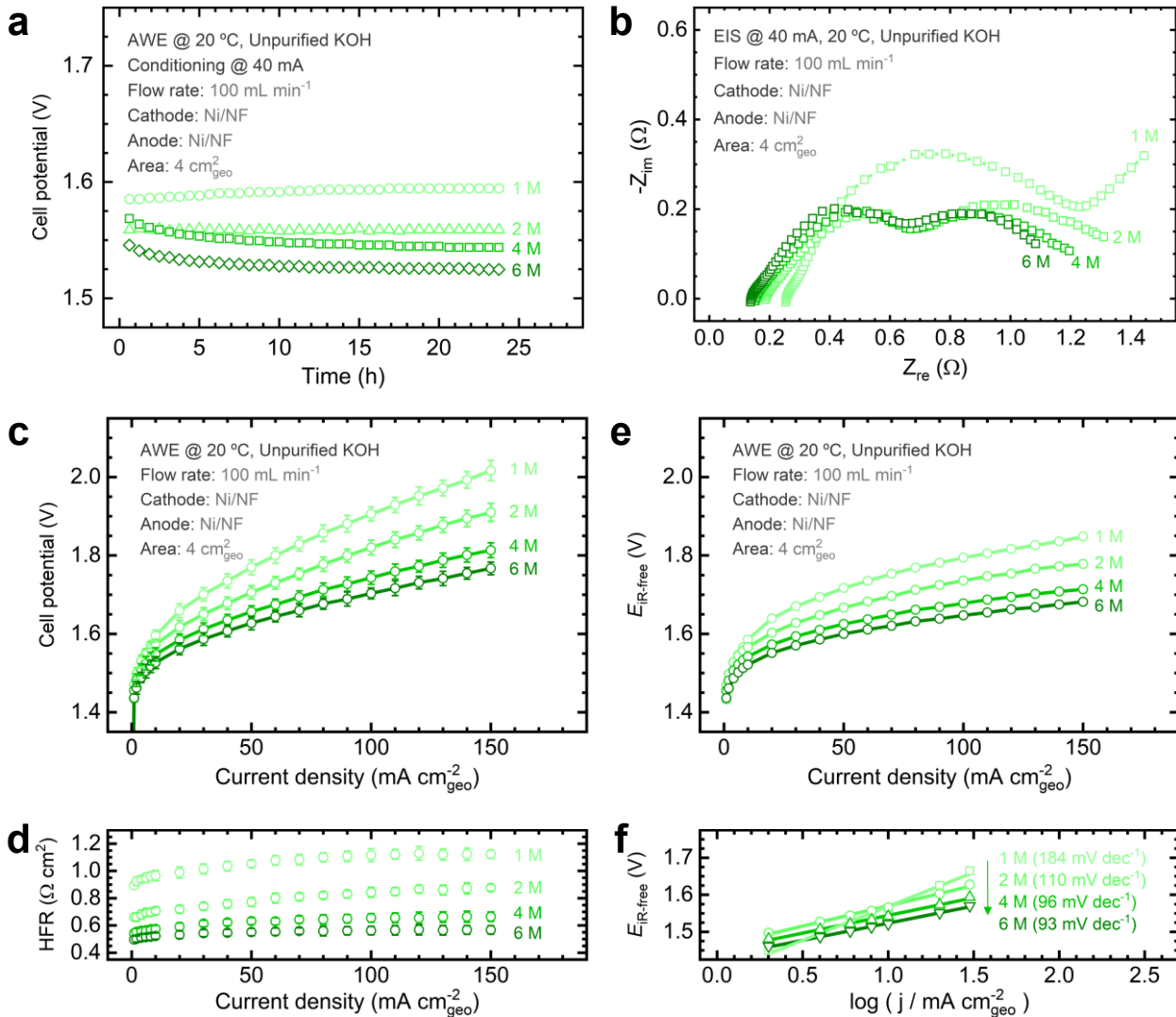


Figure S12. Electrochemical conditioning and initial assessment of the alkaline water electrolyzer operating with different KOH electrolyte concentrations: (a) electrolyzer conditioning at 40 mA for 24 h, (b) full-cell Nyquist plots, (c) full-cell polarization curve and (d) corresponding HFR values at each current step, (e) *iR*-corrected polarization curve constructed from (c) and (d), and (f) Tafel plots constructed from (e). Experimental conditions: Ni/NF anode and cathode, unpurified electrolyte at 20 °C, 100 mL·min⁻¹. Uncertainty bars indicate the standard deviation derived from three replicate measurements.

Supporting Note: **Figure S12e** has been directly reproduced from **Figure 3a** of the main manuscript to facilitate comparison between the raw and *iR*-free polarization curves. Note the decrease of the Tafel slope with increasing concentration.

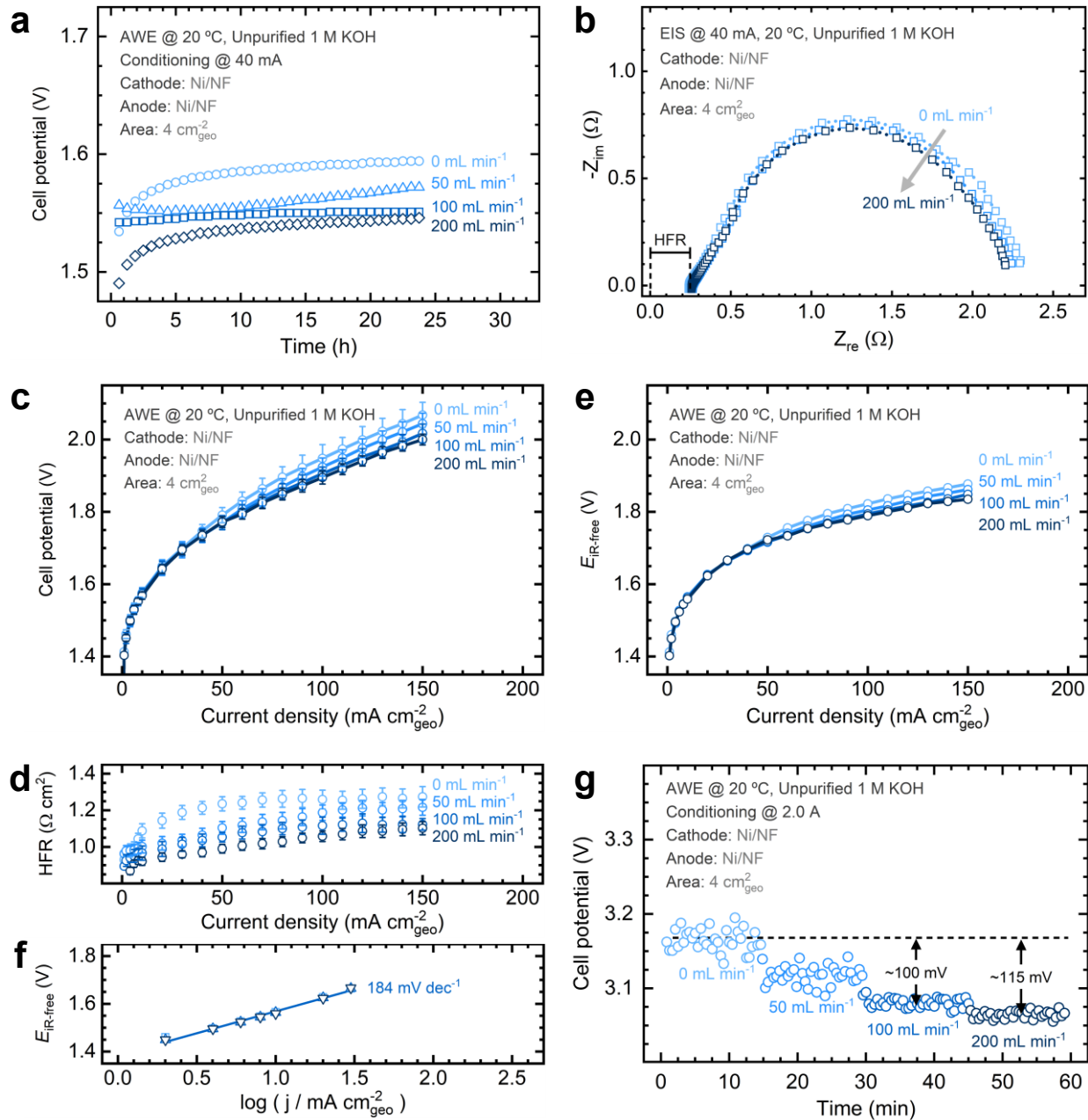


Figure S13. Electrochemical conditioning and initial assessment of the alkaline water electrolyzer operating with different electrolyte flowrates: (a) electrolyzer conditioning at 40 mA for 24 h, (b) full-cell Nyquist plots, (c) full-cell polarization curve and (d) corresponding HFR values at each current step, (e) *iR*-corrected polarization curve constructed from (c) and (d), (f) Tafel plots constructed from (e), and (g) full-cell potential at 2 A with variable flowrates. Experimental conditions: Ni/NF anode and cathode, unpurified 1 M KOH electrolyte at 20 °C. Uncertainty bars indicate the standard deviation derived from three replicate measurements.

Supporting Note: **Figure S13e** has been directly reproduced from **Figure 3b** of the main manuscript to facilitate comparison between the raw and *iR*-free polarization curves. The Tafel slope does not change with the flow rate, and the deviation of cell potentials occurs only at high current densities. This effect is attributed to mass transfer limitations due to convection.

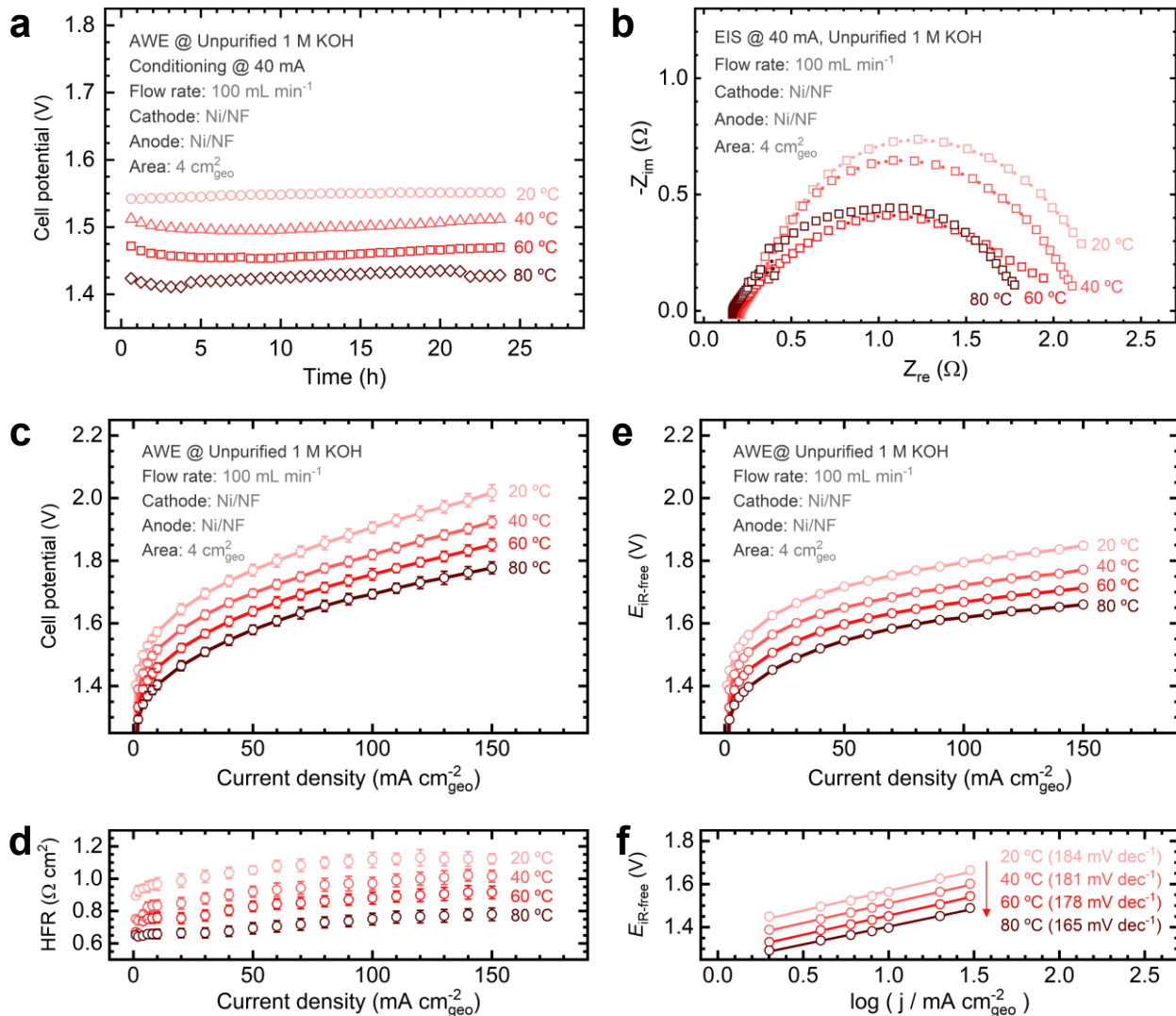


Figure S14. Electrochemical conditioning and initial assessment of the alkaline water electrolyzer operating with different electrolyte temperatures: (a) electrolyzer conditioning at 40 mA for 24 h, (b) full-cell Nyquist plots, (c) full-cell polarization curve and (d) corresponding HFR values at each current step, (e) *iR*-corrected polarization curve constructed from (c) and (d), and (f) Tafel plots constructed from (e). Experimental conditions: Ni/NF anode and cathode, unpurified 1 M KOH electrolyte, 100 mL·min⁻¹. Uncertainty bars indicate the standard deviation derived from three replicate measurements.

Supporting Note: **Figure S14e** has been directly reproduced from **Figure 3c** of the main manuscript to facilitate comparison between the raw and *iR*-free polarization curves. Note the decrease of the Tafel slope with increasing temperature.

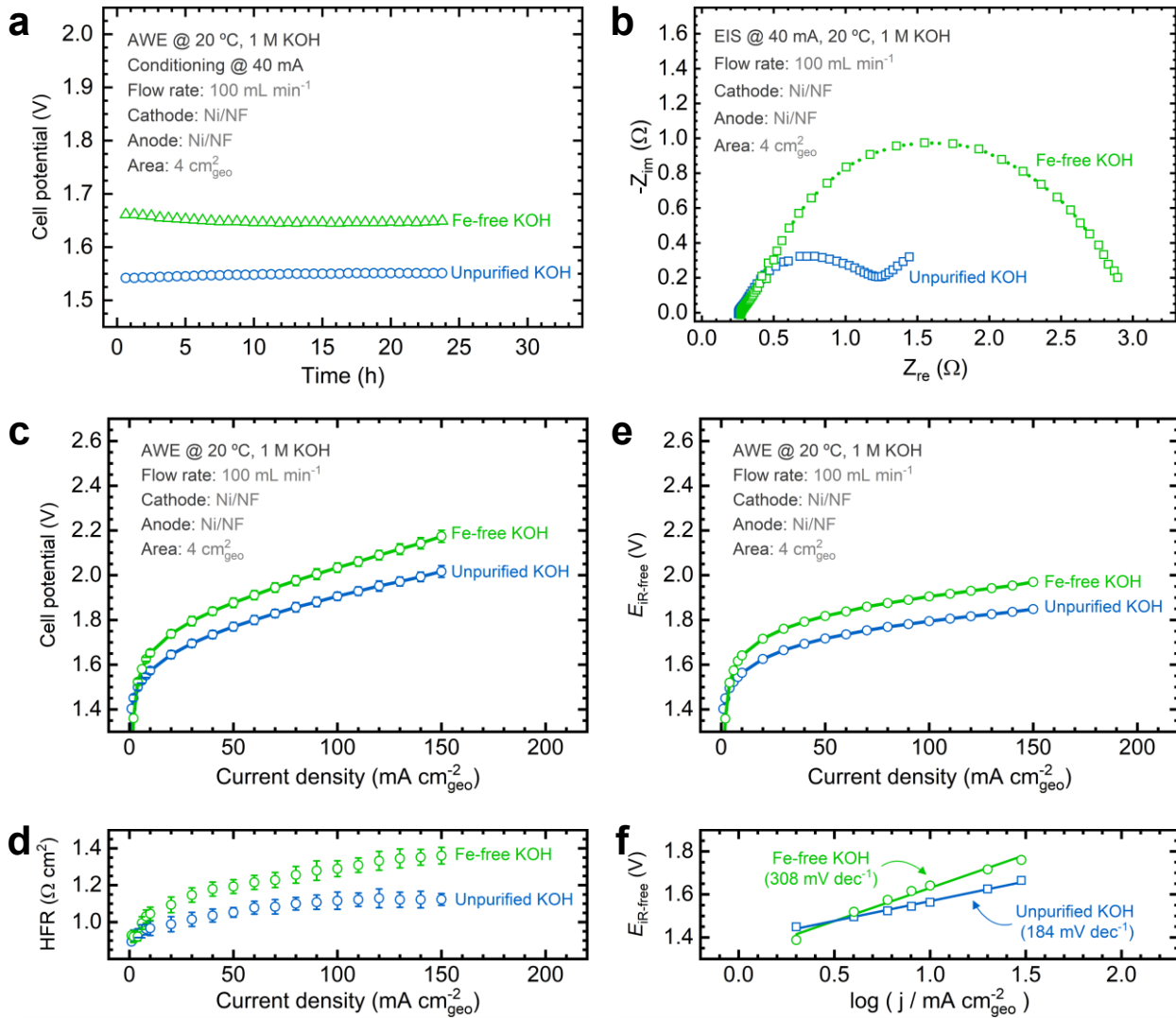


Figure S15. Electrochemical conditioning and initial assessment of the alkaline water electrolyzer operating with Fe-purified and unpurified KOH electrolytes: (a) electrolyzer conditioning at 40 mA for 24 h, (b) full-cell Nyquist plots, (c) full-cell polarization curve and (d) corresponding HFR values at each current step, (e) *iR*-corrected polarization curve constructed from (c) and (d), and (f) Tafel plots constructed from (e). Experimental conditions: Ni/NF anode and cathode, 1 M KOH electrolyte at 20 °C, 100 mL·min⁻¹. Uncertainty bars indicate the standard deviation derived from three replicate measurements.

Supporting Note: **Figure S15e** has been directly reproduced from **Figure 3d** of the main manuscript to facilitate comparison between the raw and *iR*-free polarization curves. In addition to lower cell potentials, the electrolyzer operating in unpurified KOH shows a lower Tafel slope. This effect is attributed to the OER activity enhancement due to Fe incorporation.¹

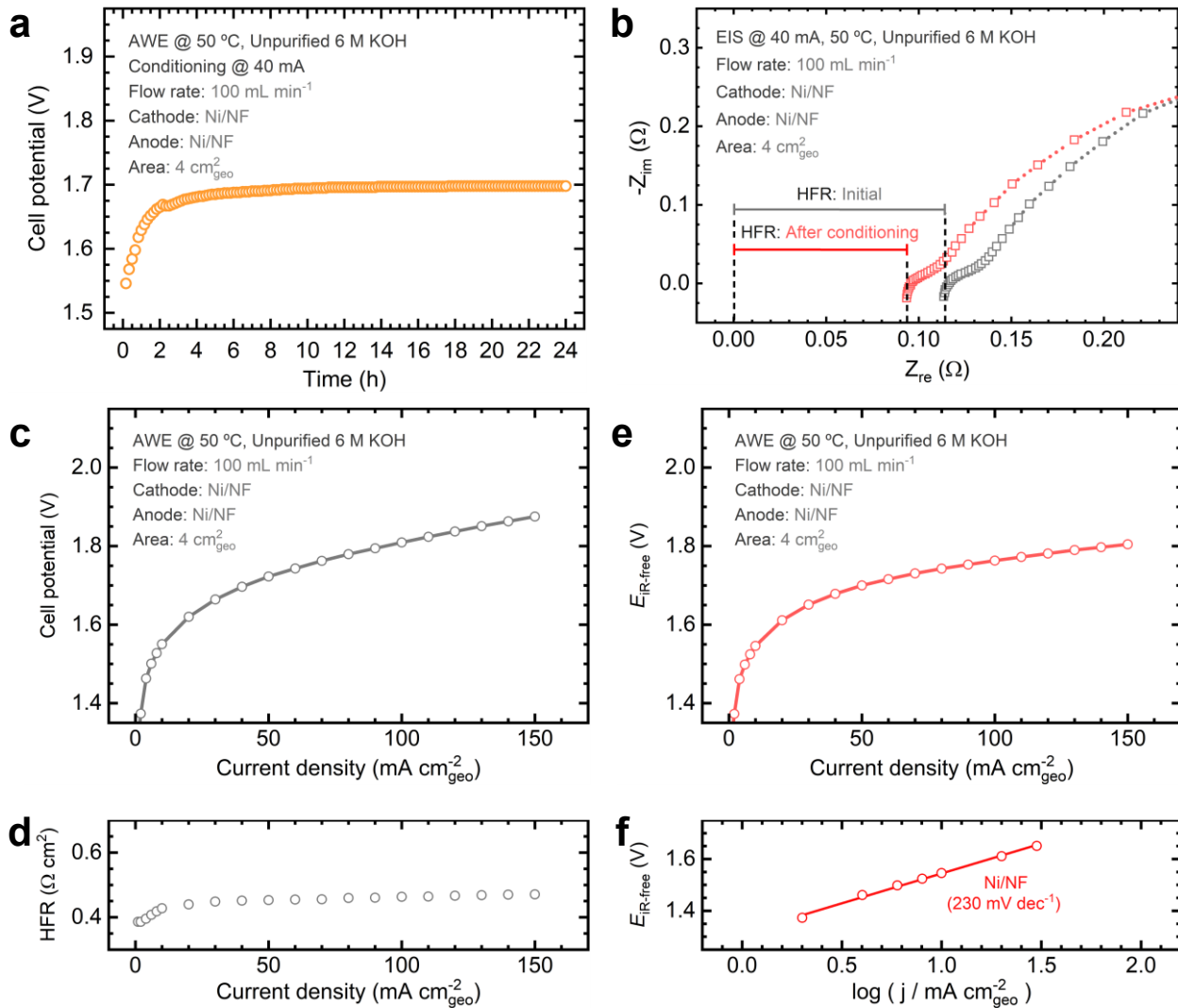


Figure S16. Electrochemical conditioning and initial assessment of the alkaline water electrolyzer operating with Ni/NF electrodes before variable current stability tests: (a) electrolyzer conditioning at 40 mA for 24 h, (b) close-up view of Nyquist plots showing the HFR region, (c) full-cell polarization curve after conditioning, (d) corresponding HFR values at each current step, (e) *iR*-corrected polarization curve constructed from (c) and (d), and (f) Tafel plot constructed from (e). Experimental conditions: unpurified 6 M KOH electrolyte at 50 °C, 100 mL·min⁻¹.

Supporting Note: As shown in **Figure S16a**, the electrode conditioning response stabilizes in about 14 h. Nyquist plots before and after testing reveal a notable HFR decrease post-conditioning (**Figure S16b**) due to a more conductive Ni oxyhydroxide film forming on the Ni/NF electrodes. The formation of this film is also evidenced by the rise in cell potential during conditioning, implying the likely formation of the less active beta phase of Ni oxyhydroxide.^{1,21}

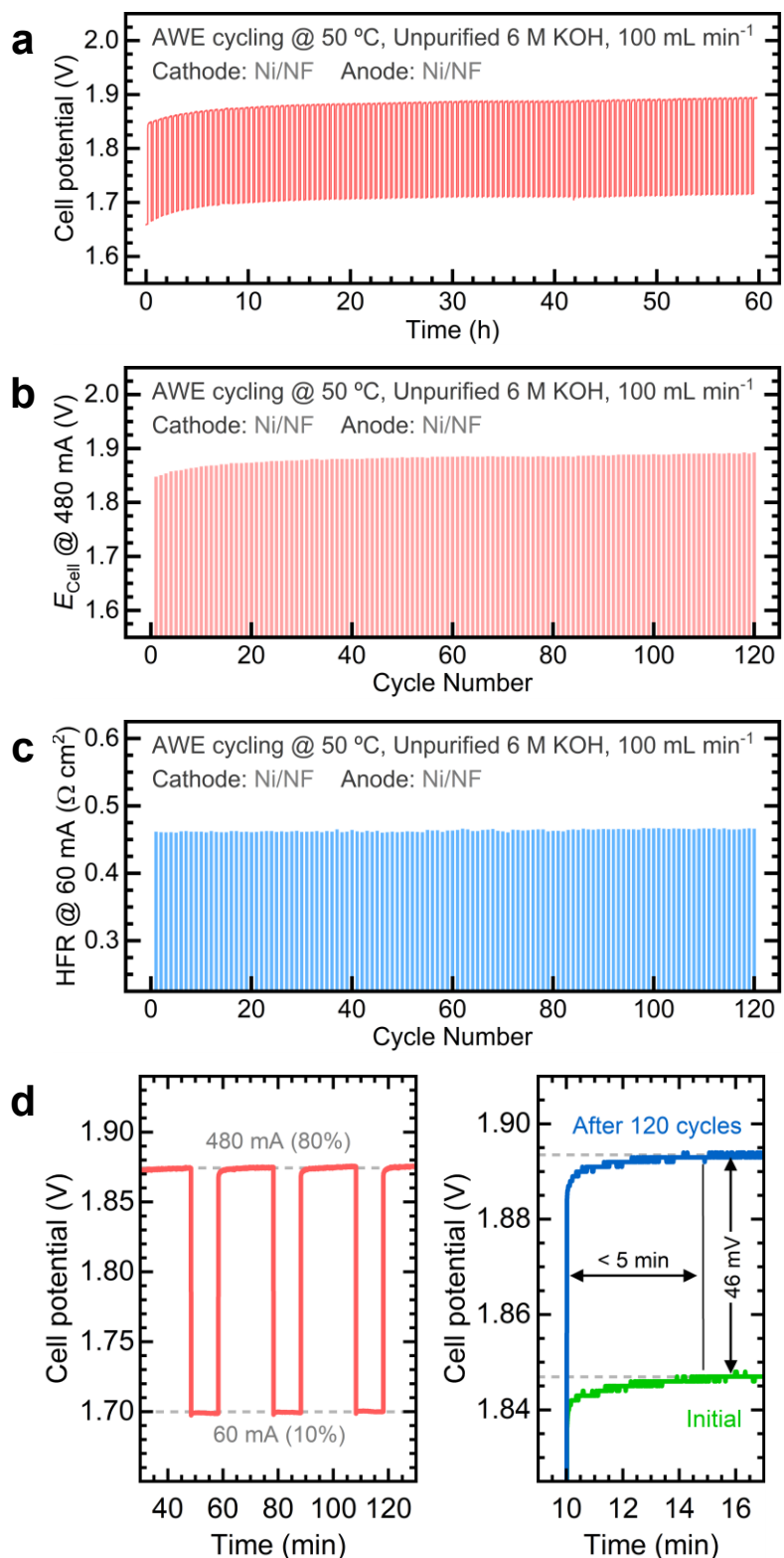


Figure S17. Alkaline water electrolysis stability tests simulating variable current conditions on Ni/NF electrodes: (a) cell potential progression over 60 h amid cycling between low and high current loads, (b) cell potential at the high load (480 mA), (c) HFR values, (d) close-up views of individual cycles at variable current.

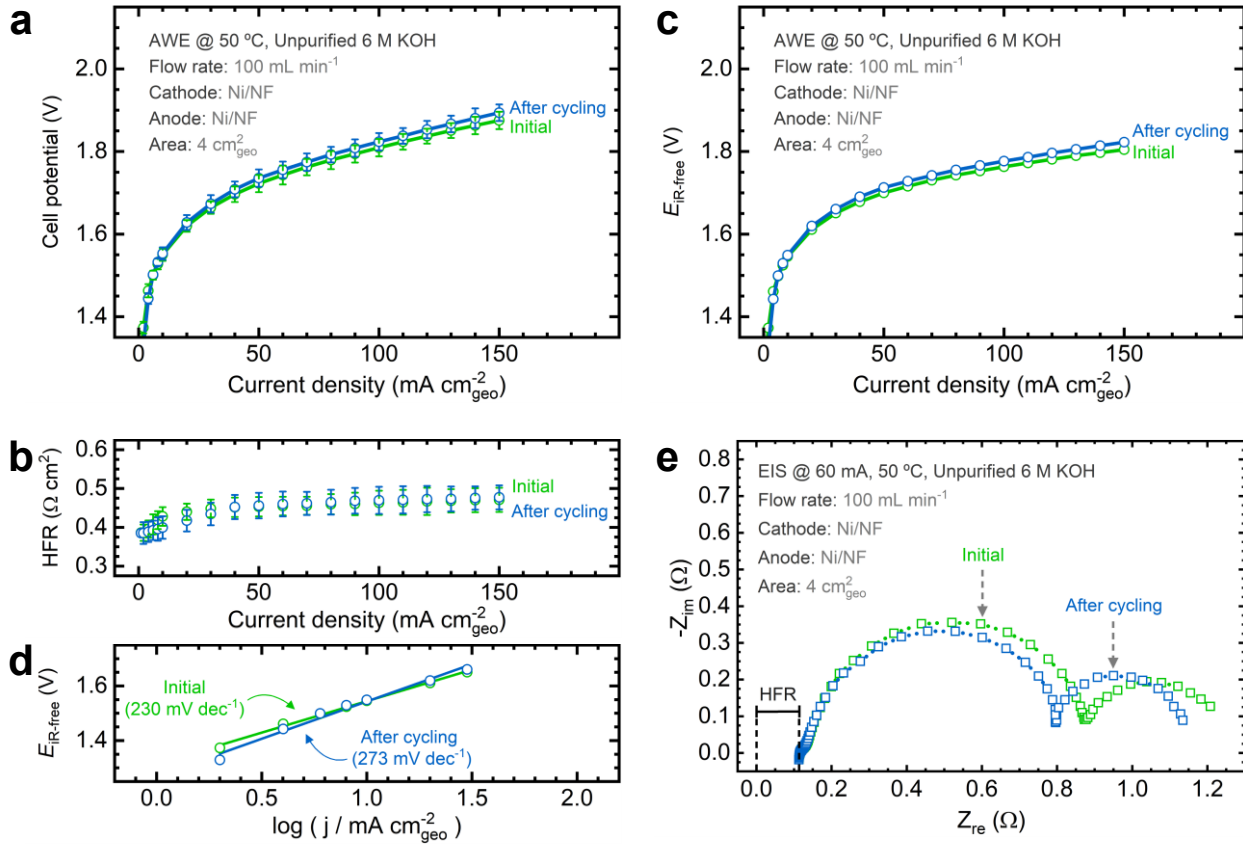


Figure S18. Electrochemical performance of the alkaline water electrolyzer operating with Ni/NF electrodes before and after variable current stability tests: (a) full-cell polarization curves, (b) corresponding HFR values at each current step, (c) iR -corrected polarization curve constructed from (a) and (b), (d) Tafel plots constructed from (c), and (e) full-cell Nyquist plots. Experimental conditions: unpurified 6 M KOH electrolyte at 50 °C, 100 mL·min⁻¹. Uncertainty bars indicate the standard deviation derived from three replicate measurements.

Supporting Note: The Ni/NF electrodes show a stable performance after approximately 28 h of alternating between low and high currents (**Figures S17a** and **b**). HFR values remain consistent (**Figure S17c**), with cell potential increasing by 46 mV after 120 cycles (**Figure S17d**). The high current step stabilizes in about 5 minutes, consistently across cycles (**Figure S17d**). Polarization curves, Nyquist plots, and Tafel slopes before and after testing show minimal changes, indicating almost negligible alterations in performance (**Figure S18**).

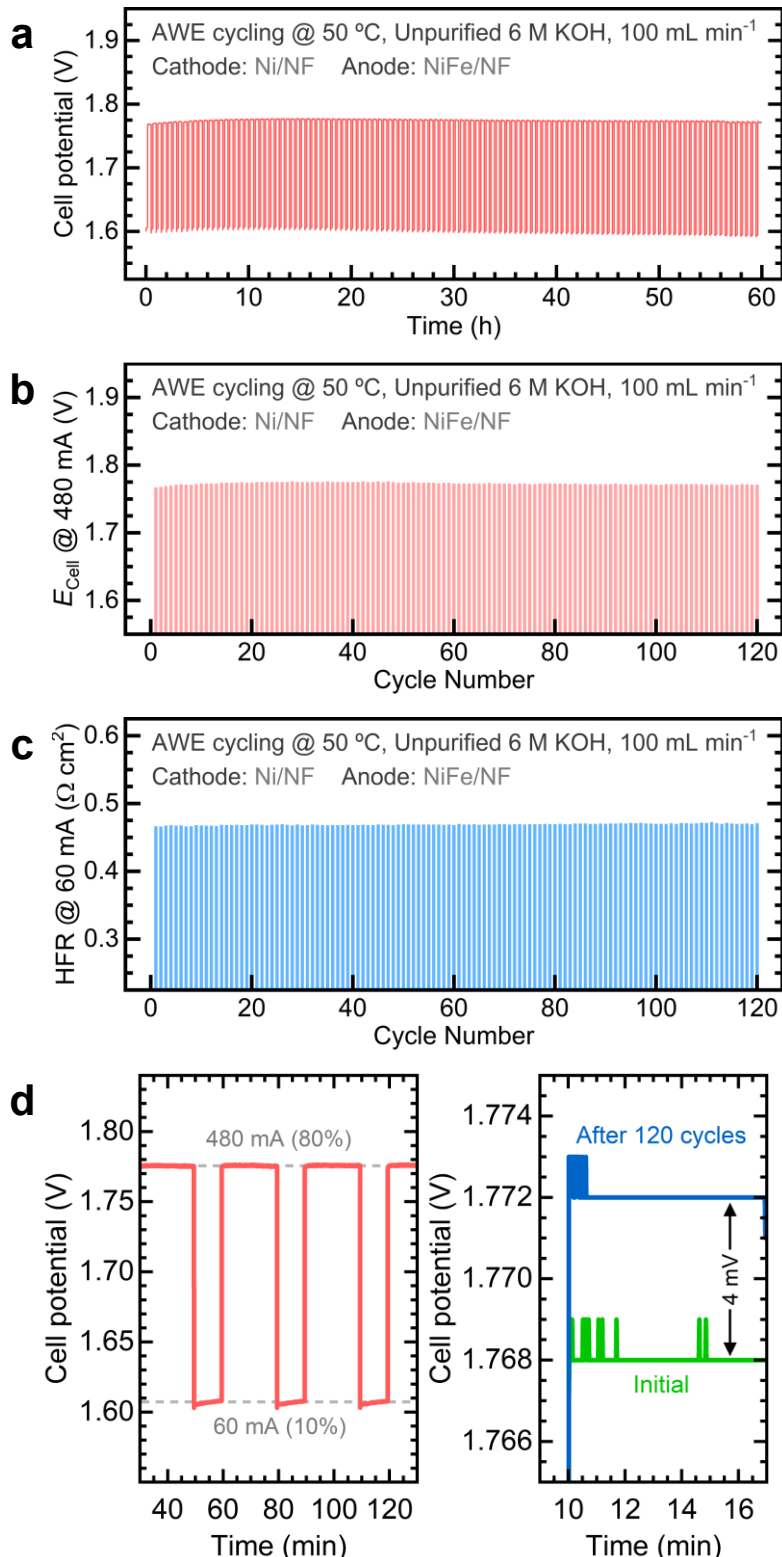


Figure S19. Alkaline water electrolysis stability tests simulating variable current conditions on NiFe/NF anodes: (a) cell potential progression over 60 h amid cycling between low and high current loads, (b) cell potential at the high load (480 mA), (c) HFR values, (d) close-up views of individual cycles at variable current.

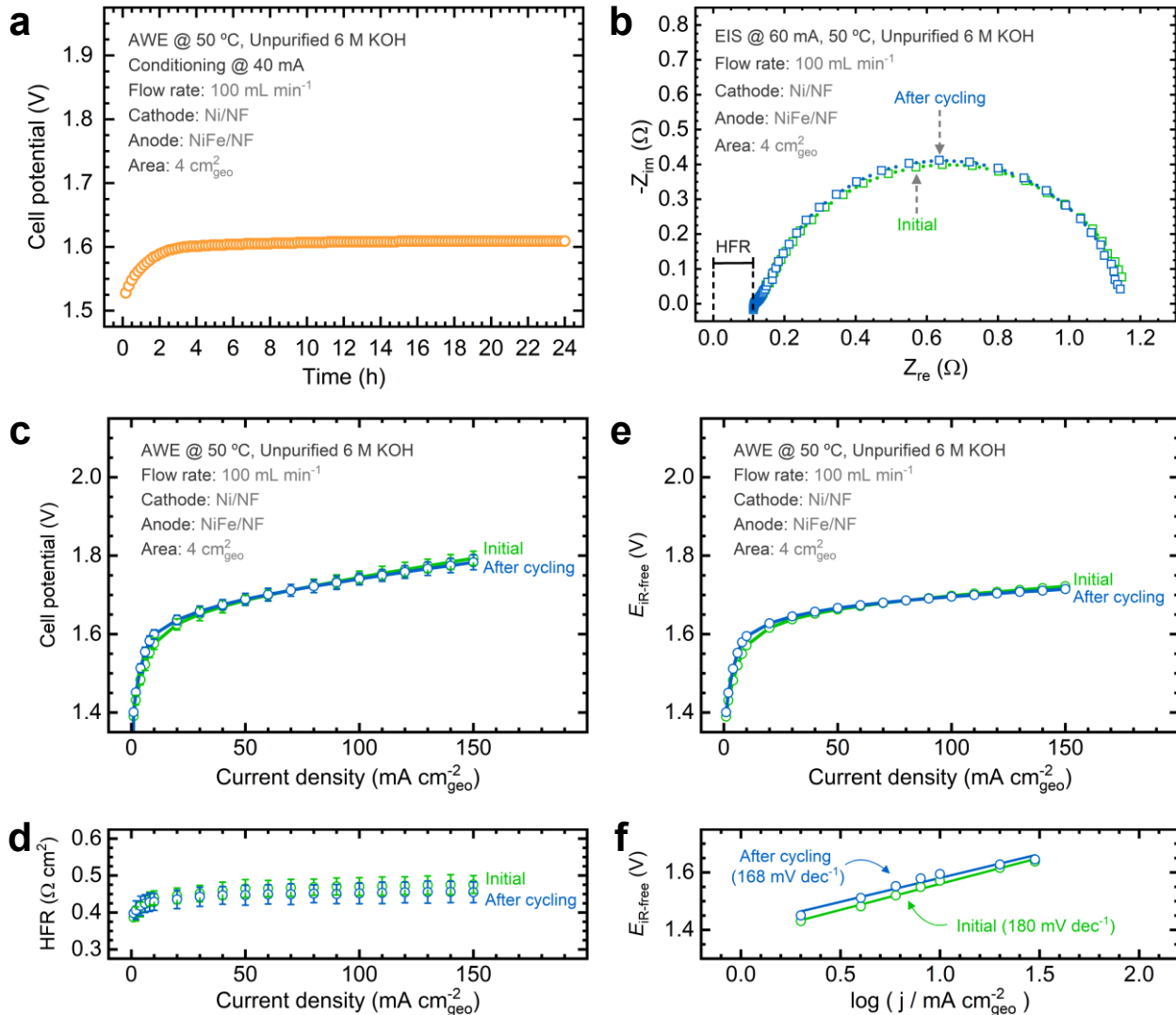


Figure S20. Electrochemical performance of the alkaline water electrolyzer operating with NiFe/NF anodes before and after variable current stability tests: (a) electrolyzer conditioning at 40 mA for 24 h, (b) full-cell Nyquist plots, (c) full-cell polarization curves, (d) corresponding HFR values at each current step, (e) *iR*-corrected polarization curve constructed from (c) and (d), and (f) Tafel plots constructed from (e). Experimental conditions: unpurified 6 M KOH electrolyte at 50 °C, 100 mL·min⁻¹. Uncertainty bars indicate the standard deviation derived from three replicate measurements.

Supporting Note: The NiFe/NF anode maintains stable performance with variable currents, showing consistent cell potential and HFR values (**Figure S19a-c**). The cell potential increases by only 4 mV after 120 cycles and responds almost instantly when switching from low to high currents (**Figure S19d**). Cell potential responses and Tafel slopes before and after testing are nearly identical (**Figure S20**). This stability is linked to the role of dissolved Fe, as the electrolyte was spiked with ~1 ppm Fe for NiFe testing, following de Groot's recommendations.^{7,8} These findings highlight the importance of dissolved Fe in stabilizing the alkaline electrolyzer's performance.

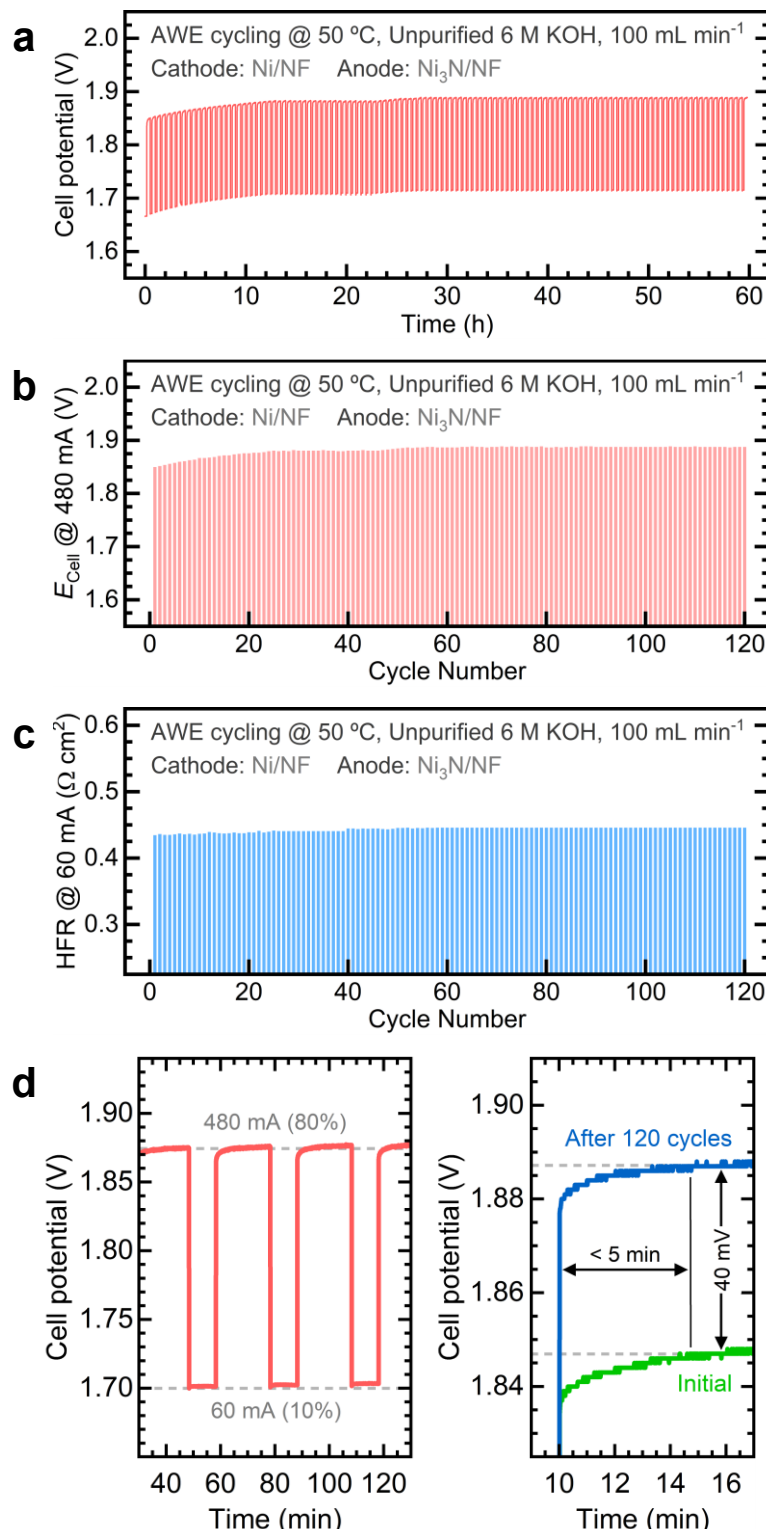


Figure S21. Alkaline water electrolysis stability tests simulating variable current conditions on Ni₃N/NF anodes: (a) cell potential progression over 60 h amid cycling between low and high current loads, (b) cell potential at the high load (480 mA), (c) HFR values, (d) close-up views of individual cycles at variable current. Note: (d) is reproduced from **Figure 4** in the main manuscript to ease comparison.

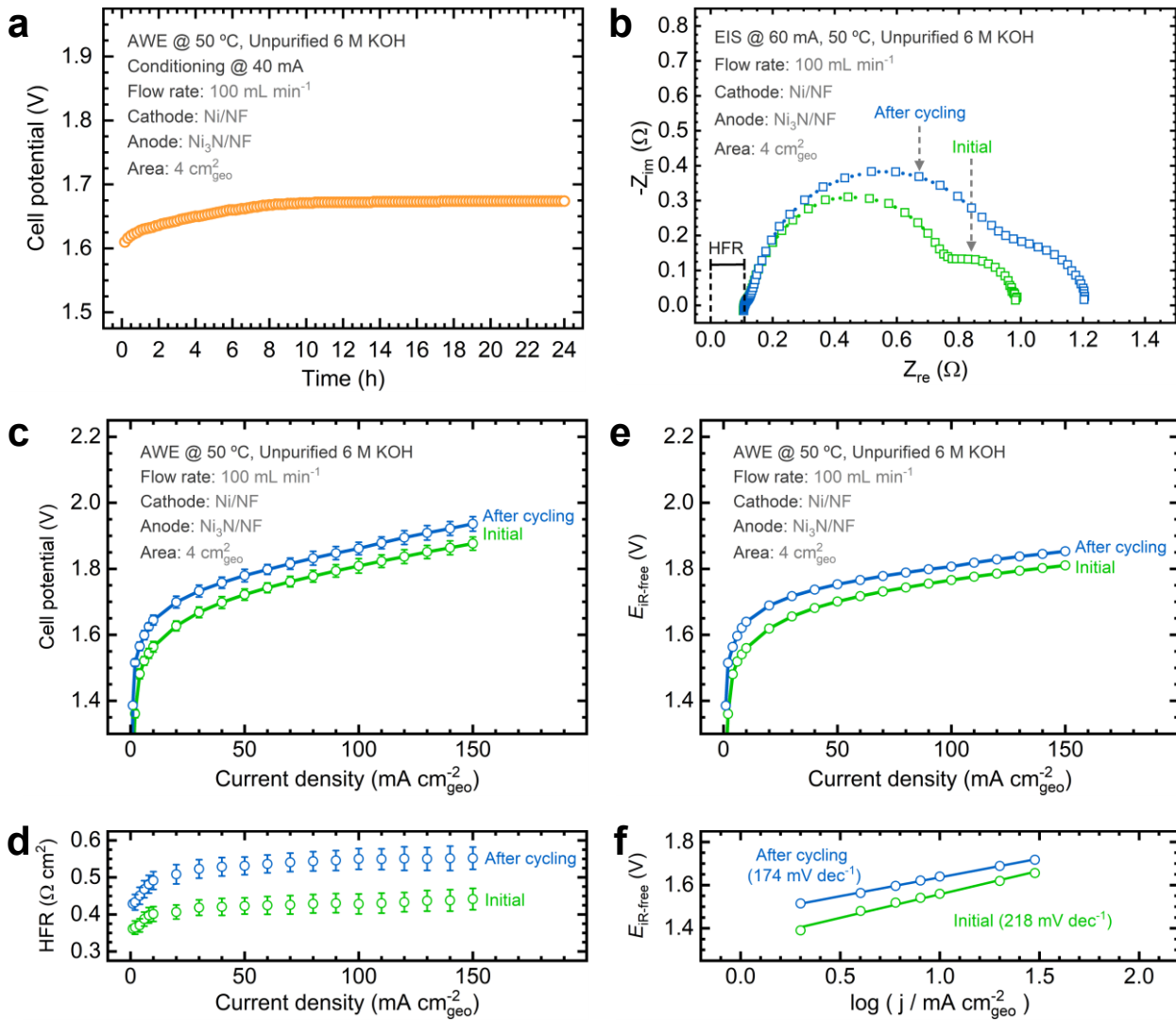


Figure S22. Electrochemical performance of the alkaline water electrolyzer operating with Ni₃N/NF anodes before and after variable current stability tests: (a) electrolyzer conditioning at 40 mA for 24 h, (b) full-cell Nyquist plots, (c) full-cell polarization curves, (d) corresponding HFR values at each current step, (e) *iR*-corrected polarization curve constructed from (c) and (d), and (f) Tafel plots constructed from (e). Experimental conditions: unpurified 6 M KOH electrolyte at 50 °C, 100 mL·min⁻¹. Uncertainty bars indicate the standard deviation derived from three replicate measurements.

Supporting Note: The Ni₃N/NF anode requires approximately 25 h to reach a steady response under alternating currents, coinciding with cell potential and HFR responses (**Figure S21a-c**). The cell potential increases by 40 mV after 120 cycles, and the high current response stabilizes in roughly 5 min, similar to the Ni/NF electrode (**Figure S21d**). Polarization curves and Nyquist plots before and after testing display significant differences (**Figure S20**), reflecting changes in the charge transfer resistance of the materials. The Tafel slope decreases significantly after cycling (**Figure S22f**), which could be attributed to Fe incorporation. This behavior is linked to the precatalytic effect of Ni₃N under OER conditions, a subject extensively studied by our group.^{14,22}

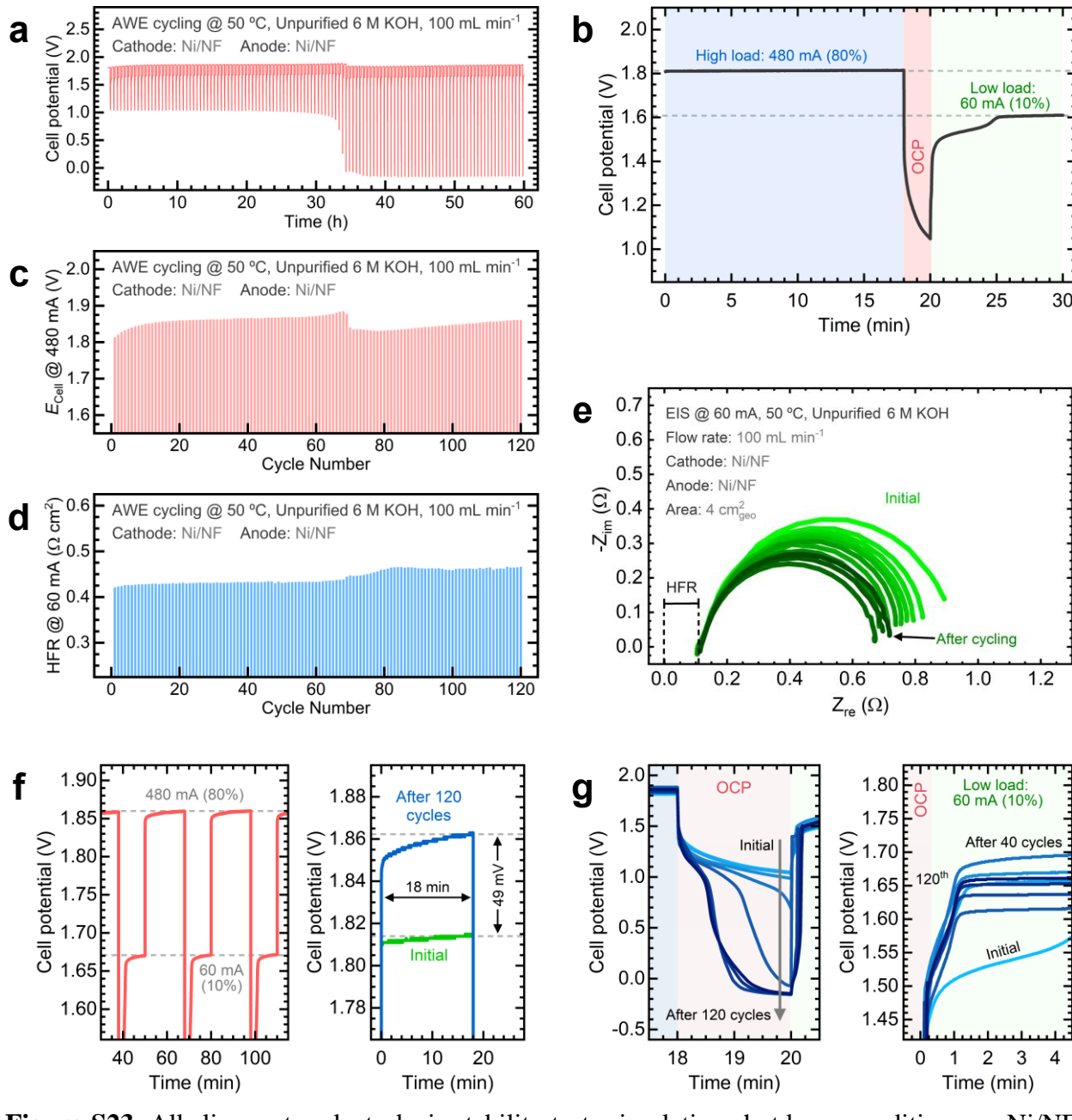


Figure S23. Alkaline water electrolysis stability tests simulating shutdown conditions on Ni/NF electrodes: (a) cell potential progression over 60 h amid cycling between multiple current loads and a shutdown step, (b) magnified snapshot of a single cycle depicting the shutdown event at OCP, (c) cell potential at the high load (480 mA), (d) HFR values, (e) Nyquist plots over cycling, (f) close-up views of individual cycles at variable current, and (g) close-up views of OCP and low-load steps comparing the cell potential progression over 120 cycles.

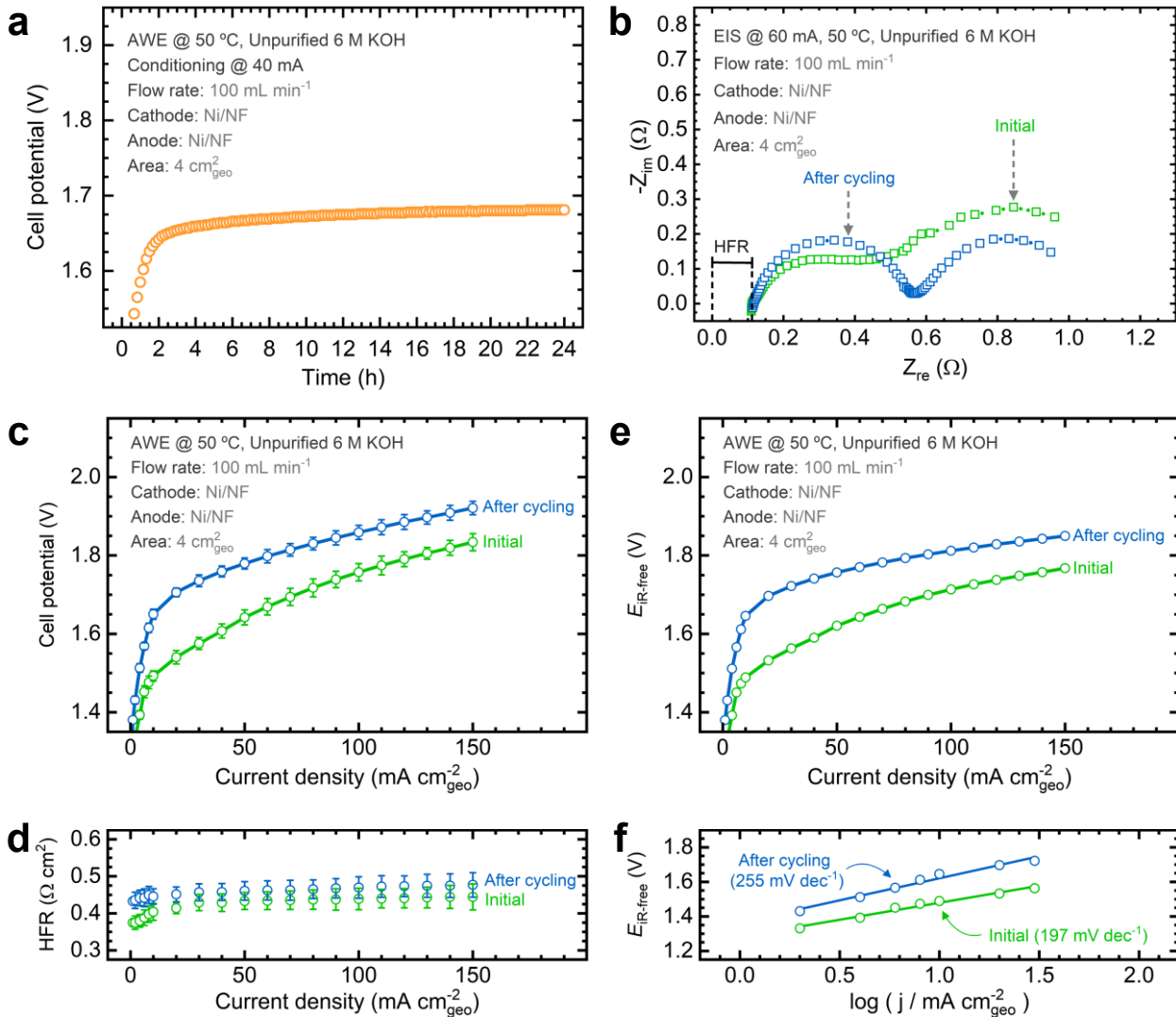


Figure S24. Electrochemical performance of the alkaline water electrolyzer operating with Ni/NF electrodes before and after simulated shutdown stability tests: (a) electrolyzer conditioning at 40 mA for 24 h, (b) full-cell Nyquist plots, (c) full-cell polarization curves, (d) corresponding HFR values at each current step, (e) *iR*-corrected polarization curve constructed from (c) and (d), and (f) Tafel plots constructed from (e). Experimental conditions: unpurified 6 M KOH electrolyte at 50 °C, 100 mL·min⁻¹. Uncertainty bars indicate the standard deviation derived from three replicate measurements.

Supporting Note: The Ni/NF electrodes exhibit notable fluctuations in the alternating current response, especially after ~34 h (**Figure S23a**). The cell potential and HFR responses also change significantly after this event (**Figures S23c and d**), with the Nyquist plot revealing substantial changes in the charge transfer resistance (**Figure S23e**). While cell potential increases by only 49 mV after cycling, stabilization times extend (**Figure S23f**). The OCP turns more negative after 34 h, with notable fluctuations in cell potential at low currents (**Figure S23g**). Polarization curves and Nyquist plots change notably before and after cycling, and the Tafel slope increases (**Figure S24**). These findings suggest a continuous oxidation and reduction of the Ni/NF cathode between Ni(OH)_2 and Ni phases due to reverse-current flow, affecting electronic conductivity.²³ Negative OCP potentials might also cause transient Ni dissolution, according to Pourbaix diagrams.²⁴ This condition might also cause Fe impurity redissolution, which could explain the increase of the Tafel slope and cell potential.

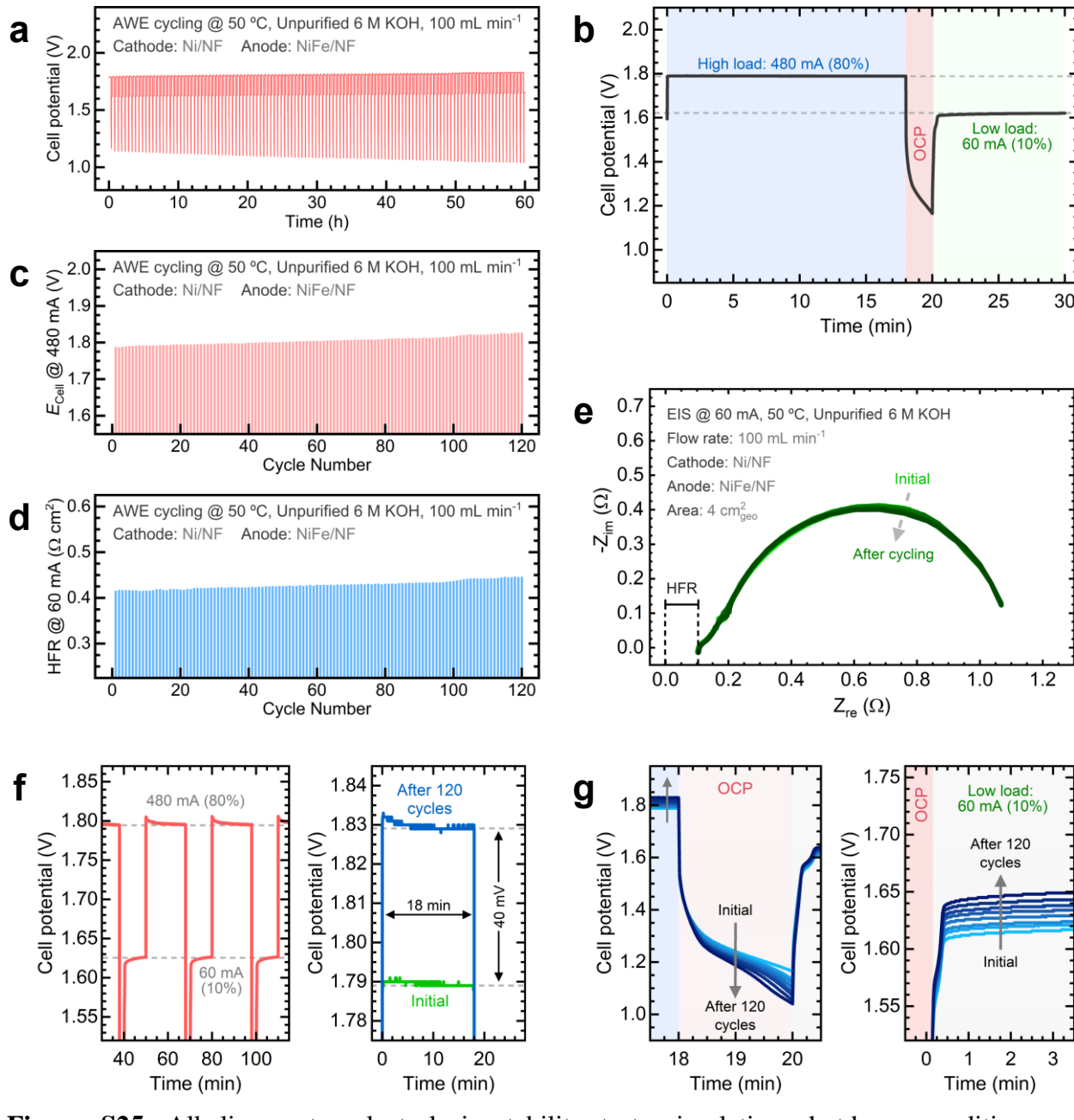


Figure S25. Alkaline water electrolysis stability tests simulating shutdown conditions on NiFe/NF anodes: (a) cell potential progression over 60 h amid cycling between multiple current loads and a shutdown step, (b) magnified snapshot of a single cycle depicting the shutdown event at OCP, (c) cell potential at the high load (480 mA), (d) HFR values, (e) Nyquist plots over cycling, (f) close-up views of individual cycles at variable current, and (g) close-up views of OCP and low-load steps comparing the cell potential progression over 120 cycles. Note: (g) is reproduced from **Figure 4** of the main manuscript to ease comparison.

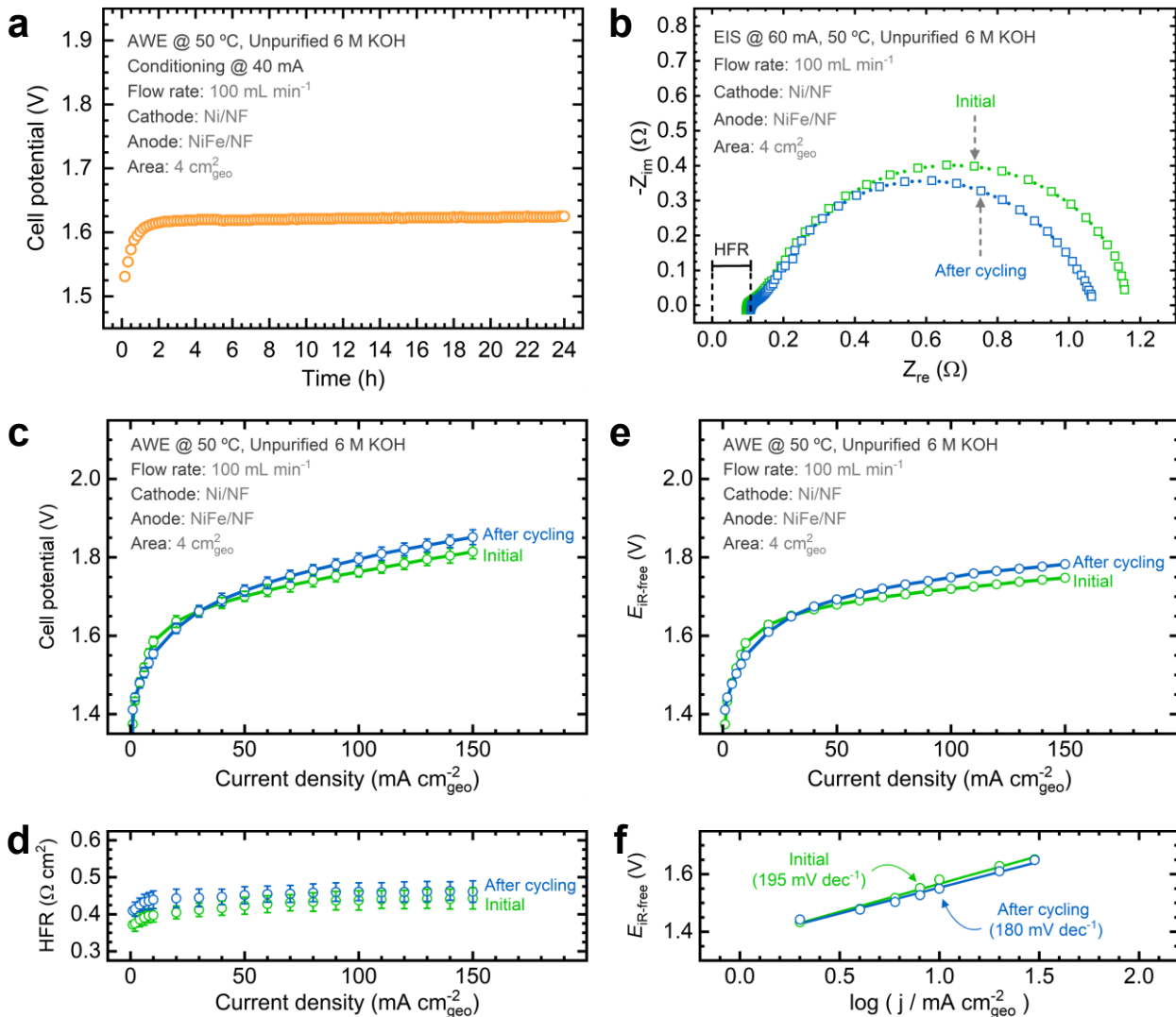


Figure S26. Electrochemical performance of the alkaline water electrolyzer operating with NiFe/NF anodes before and after simulated shutdown stability tests: (a) electrolyzer conditioning at 40 mA for 24 h, (b) full-cell Nyquist plots, (c) full-cell polarization curves, (d) corresponding HFR values at each current step, (e) *iR*-corrected polarization curve constructed from (c) and (d), and (f) Tafel plots constructed from (e). Experimental conditions: unpurified 6 M KOH electrolyte at 50 °C, 100 mL·min⁻¹. Uncertainty bars indicate the standard deviation derived from three replicate measurements.

Supporting Note: The NiFe/NF anode shows a more stable response with alternating currents, maintaining a positive OCP throughout the test (**Figure S25a**). However, there is a subtle but steady decrease in OCP and a corresponding rise in cell potential and HFR (**Figure S25a, c, and d**). Nyquist plots remain unchanged (**Figure S25e**), and pre- and post-cycling performance looks similar (**Figure S26**). The cell potential increases ~40 mV, showing a less stable response at high currents after cycling (**Figure S25f** and **S26f**), with a gradual OCP decrease, cell potential rise at low currents, and Tafel slope decrease (**Figure S25g**). This observed behavior could stem from the ongoing dissolution of Ni or Fe. Fe dendrites, known to form when Fe is added to the electrolyte, may redissolve during shutdown steps.⁸ This phenomenon demands additional investigation.

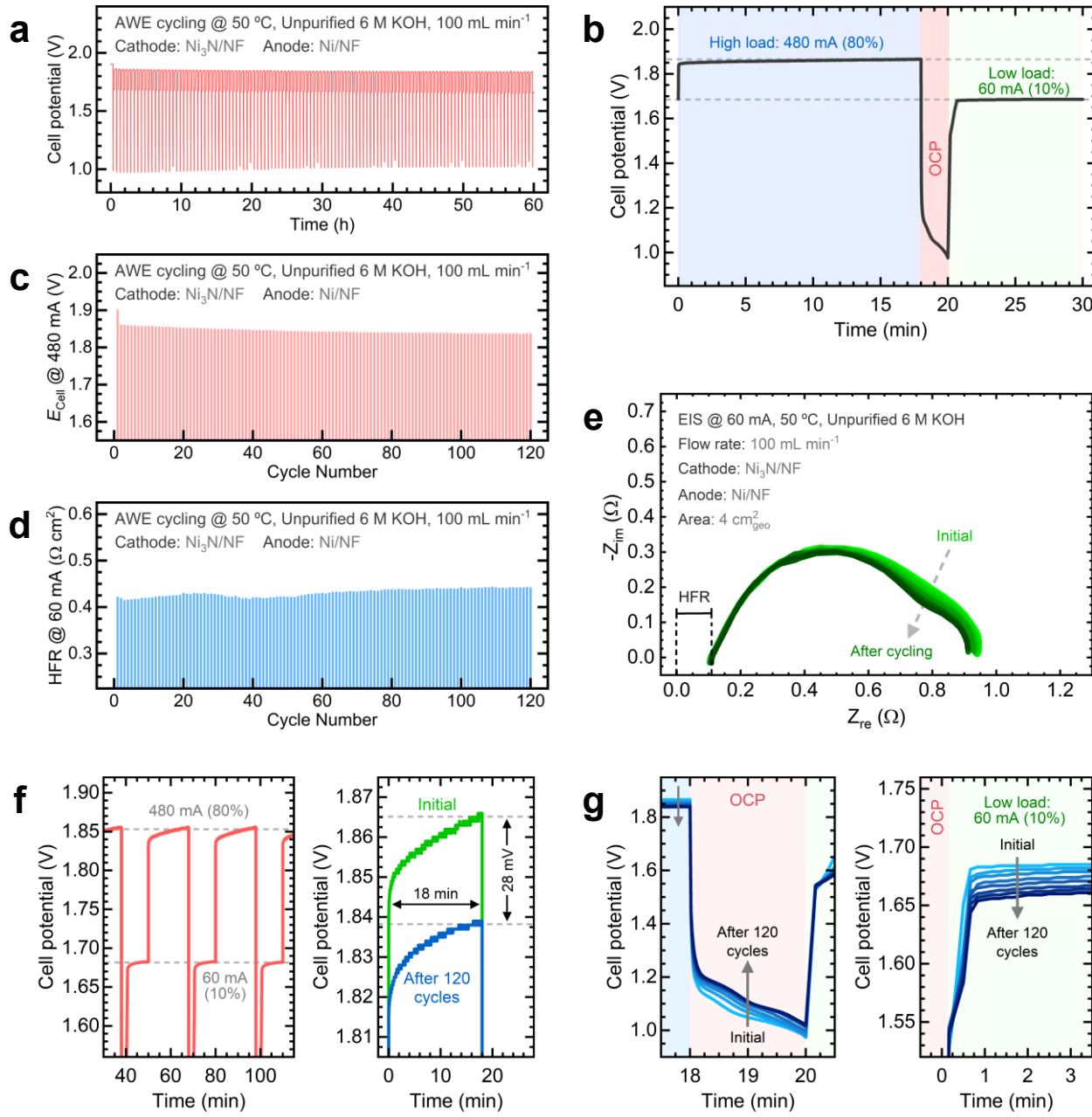


Figure S27. Alkaline water electrolysis stability tests simulating shutdown conditions on Ni₃N/NF cathodes: (a) cell potential progression over 60 h amid cycling between multiple current loads and a shutdown step, (b) magnified snapshot of a single cycle depicting the shutdown event at OCP, (c) cell potential at the high load (480 mA), (d) HFR values, (e) Nyquist plots over cycling, (f) close-up views of individual cycles at variable current, and (g) close-up views of OCP and low-load steps comparing the cell potential progression over 120 cycles.

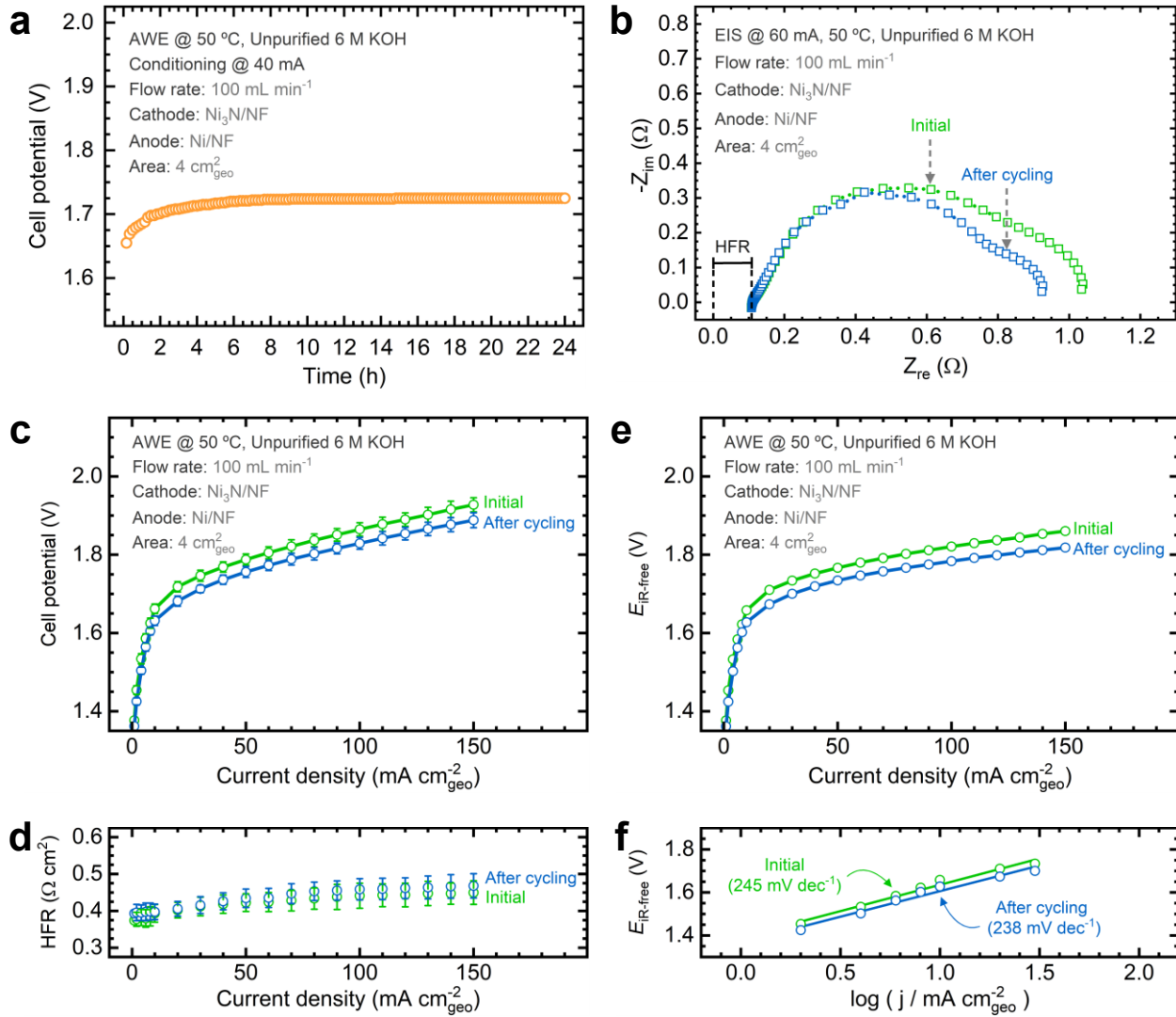


Figure S28. Electrochemical performance of the alkaline water electrolyzer operating with Ni₃N/NF cathodes before and after simulated shutdown stability tests: (a) electrolyzer conditioning at 40 mA for 24 h, (b) full-cell Nyquist plots, (c) full-cell polarization curves, (d) corresponding HFR values at each current step, (e) iR_{free}-corrected polarization curve constructed from (c) and (d), and (f) Tafel plots constructed from (e). Experimental conditions: unpurified 6 M KOH electrolyte at 50 °C, 100 mL·min⁻¹. Uncertainty bars indicate the standard deviation derived from three replicate measurements.

Supporting Note: Unlike the rest of the electrodes, the performance of the Ni₃N/NF cathode improves after cycling. The Ni₃N/NF cathode shows a stable response under alternating currents, with minor cell potential and HFR changes (**Figures S27a, c, and d**). Nyquist plots show a subtle decrease in the charge transfer resistance (**Figure S27e**), along with slight changes in the performance after cycling (**Figure S28**). The cell potential decreases by 28 mV, with a slight OCP increase and cell potential drop at low currents (**Figures S27f and g**). The Tafel slope slightly decreases after testing (**Figure S28f**). These results suggest that reverse currents during shutdown may activate self-healing mechanisms, potentially related to the formation of Ni hydroxide domains on the surface of Ni₃N cathodes.²²

Table S1. Performance metrics for tested anodes in fluctuating current stability tests.

Anode composition	Ni/NF	Ni ₃ N/NF	NiFe/NF
T _{cell} (°C)	50	50	50
E _{cond} @ 40 mA (V)	1.698	1.674	1.609
HFR _{cond} @ 60 mA (Ω·cm ²)	0.374	0.433	0.454
E _{cell,initial} @ 10 mA·cm ⁻² (V)	1.546	1.560	1.571
E _{cell,after} @ 10 mA·cm ⁻² (V)	1.549	1.640	1.595
E _{cell,initial} @ 100 mA·cm ⁻² (V)	1.763	1.766	1.698
E _{cell,after} @ 100 mA·cm ⁻² (V)	1.777	1.807	1.695
b _{exp,initial} (mV·dec ⁻¹)	230.6	218.1	180.1
b _{exp,after} (mV·dec ⁻¹)	273.3	174.4	168.3
b _{HER} @ T (mV·dec ⁻¹)	128.1	128.1	128.1
b _{OER,initial} (mV·dec ⁻¹)	102.5	90.0	52.0
b _{OER,after} (mV·dec ⁻¹)	145.2	46.3	40.2
HFR _{stab,1st} @ 60 mA (Ω·cm ²)	0.463	0.436	0.468
HFR _{stab,120th} @ 60 mA (Ω·cm ²)	0.467	0.447	0.472
E _{cell,1st} @ 480 mA (V)	1.849	1.851	1.768
E _{cell,120th} @ 480 mA (V)	1.894	1.889	1.772
t _{stab,1st} @ 480 mA (s)	266	282	110
t _{stab,120th} @ 480 mA (s)	297	240	42

Table S2. Performance metrics for tested anodes in reverse current stability tests.

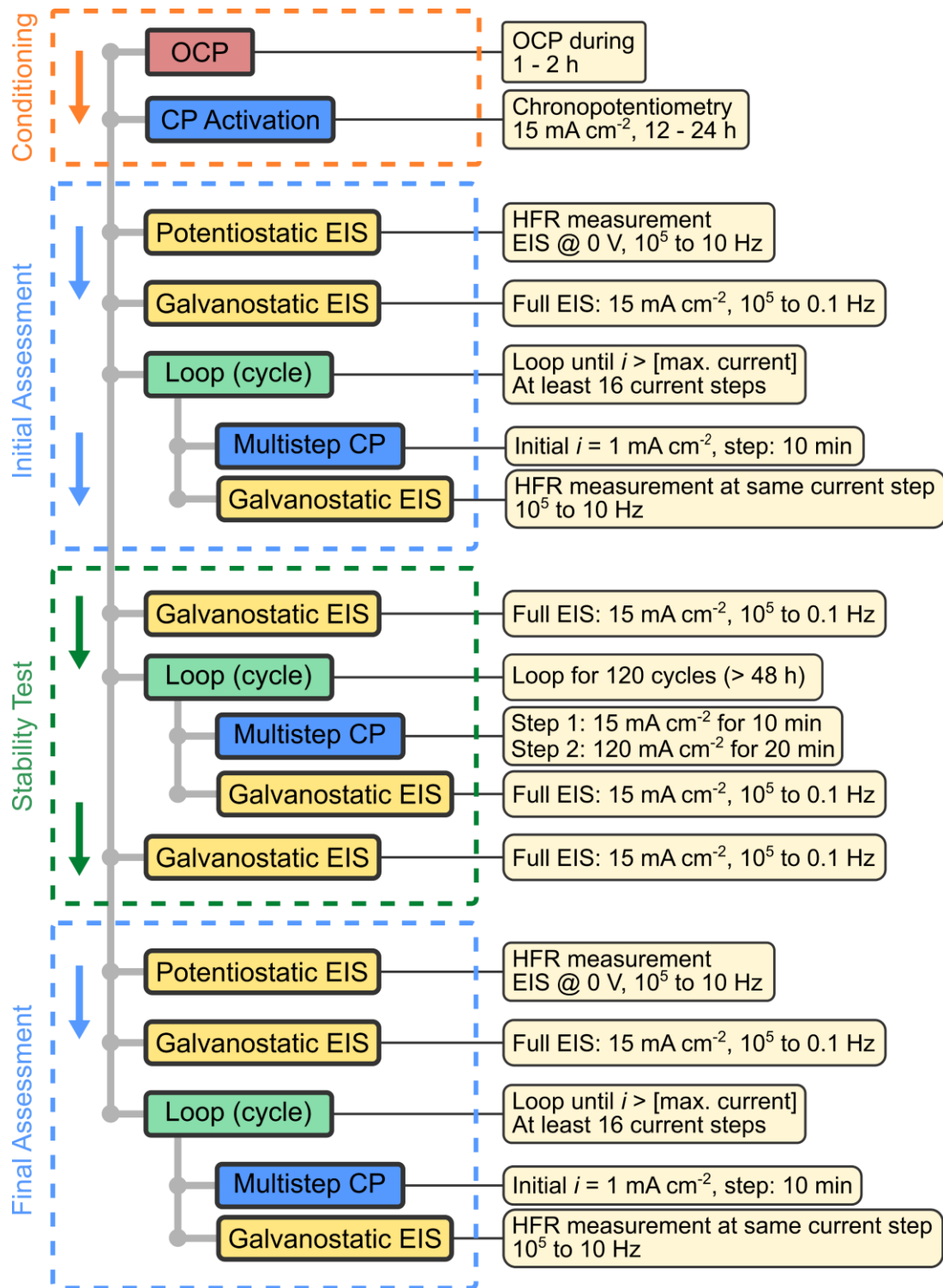
Anode composition	Ni/NF	Ni ₃ N/NF	NiFe/NF
T _{cell} (°C)	50	50	50
E _{cond} @ 40 mA (V)	1.681	1.725	1.625
HFR _{cond} @ 60 mA (Ω·cm ²)	0.401	0.429	0.381
E _{cell,initial} @ 10 mA·cm ⁻² (V)	1.489	1.658	1.581
E _{cell,after} @ 10 mA·cm ⁻² (V)	1.646	1.627	1.550
E _{cell,initial} @ 100 mA·cm ⁻² (V)	1.713	1.821	1.719
E _{cell,after} @ 100 mA·cm ⁻² (V)	1.812	1.783	1.749
b _{exp,initial} (mV·dec ⁻¹)	196.8	244.8	194.7
b _{exp,after} (mV·dec ⁻¹)	255.0	238.0	180.1
b _{HER} @ T (mV·dec ⁻¹)	128.1	128.1	128.1
b _{OER,initial} (mV·dec ⁻¹)	68.7	116.7	66.6
b _{OER,after} (mV·dec ⁻¹)	126.9	109.9	52.0
HFR _{stab,1st} @ 60 mA (Ω·cm ²)	0.422	0.423	0.417
HFR _{stab,120th} @ 60 mA (Ω·cm ²)	0.468	0.443	0.447
E _{cell,1st} @ 480 mA (V)	1.815	1.903	1.789
E _{cell,120th} @ 480 mA (V)	1.862	1.839	1.828
t _{stab,1st} @ 480 mA (s)	710	983	770
t _{stab,120th} @ 480 mA (s)	866	978	656

Supporting Note: Abbreviations and notes for **Tables S1** and **S2**.

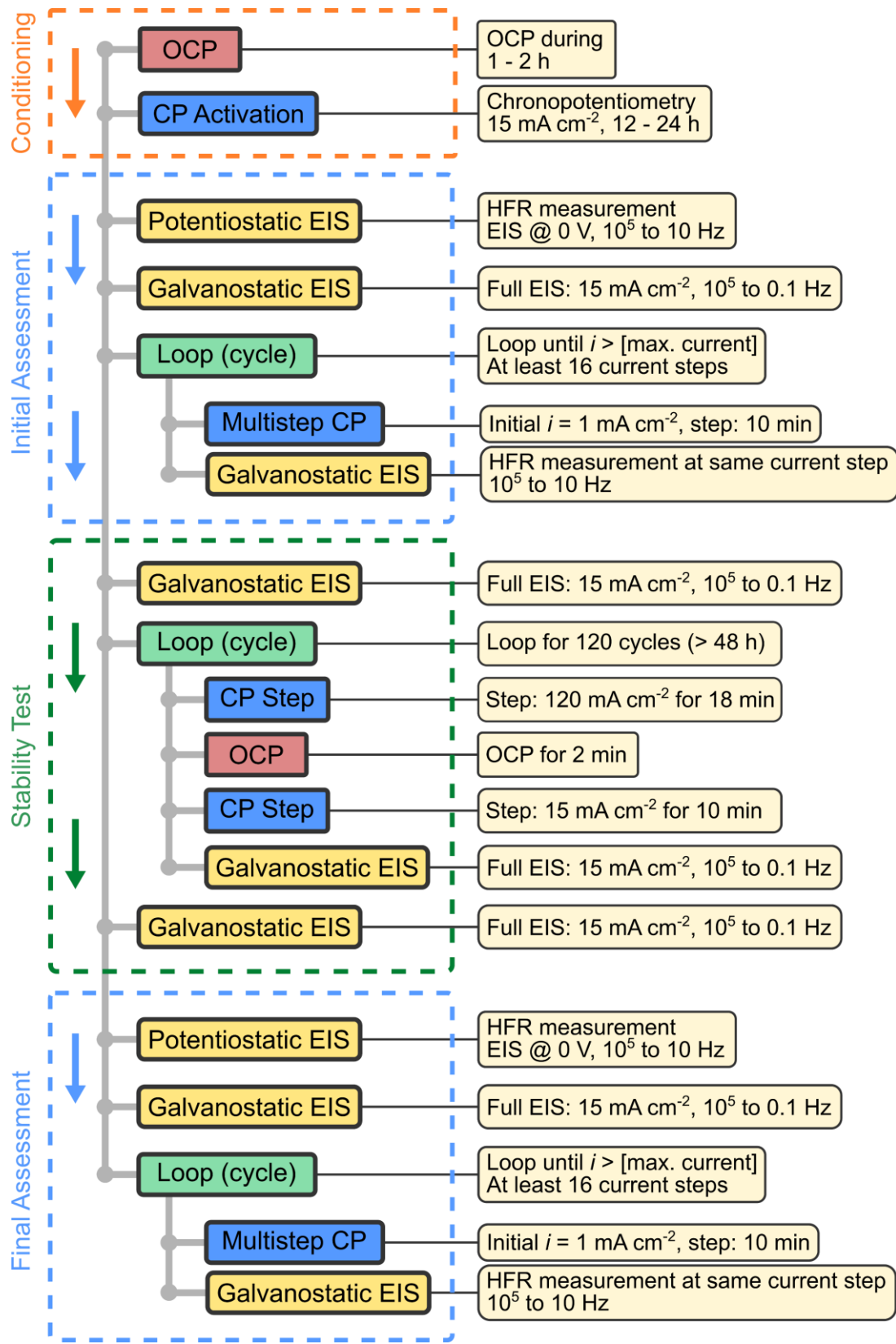
T_{cell}	Operating temperature.
$E_{\text{cond}} @ 40 \text{ mA}$	Stable cell potential after electrochemical conditioning at 40 mA for 24 hours.
$\text{HFR}_{\text{cond}} @ 60 \text{ mA}$	HFR value at 60 mA after electrochemical conditioning for 24 hours.
$E_{\text{cell,initial}} @ 10 \text{ mA}\cdot\text{cm}^{-2}$	Cell potential at $10 \text{ mA}\cdot\text{cm}^{-2}$ from the initial polarization curve (iR -corrected).
$E_{\text{cell,after}} @ 10 \text{ mA}\cdot\text{cm}^{-2}$	Cell potential at $10 \text{ mA}\cdot\text{cm}^{-2}$ from the polarization curve after the stability test (iR -corrected).
$E_{\text{cell,initial}} @ 100 \text{ mA}\cdot\text{cm}^{-2}$	Cell potential at $100 \text{ mA}\cdot\text{cm}^{-2}$ from the initial polarization curve (iR -corrected).
$E_{\text{cell,after}} @ 100 \text{ mA}\cdot\text{cm}^{-2}$	Cell potential at $100 \text{ mA}\cdot\text{cm}^{-2}$ from the polarization curve after the stability test (iR -corrected).
$b_{\text{exp,initial}}$	Experimental Tafel slope from the initial polarization curve.
$b_{\text{exp,after}}$	Experimental Tafel slope from the polarization curve after the stability test.
$b_{\text{HER}} @ T$	Theoretical Tafel slope for the HER at the operating temperature, calculated using Eq. 5.
$b_{\text{OER,initial}}$	Tafel slope for the OER from the initial polarization curve, calculated using Eq. 4.
$b_{\text{OER,after}}$	Tafel slope for the OER from the polarization curve after the stability test, calculated using Eq. 4.
$\text{HFR}_{\text{stab,1st}} @ 60 \text{ mA}$	HFR value at 60 mA after the first stability cycle.
$\text{HFR}_{\text{stab,120th}} @ 60 \text{ mA}$	HFR value at 60 mA after the last stability cycle.
$E_{\text{cell,1st}} @ 480 \text{ mA}$	Cell potential at the high load step after the first stability cycle.
$E_{\text{cell,120th}} @ 480 \text{ mA}$	Cell potential at the high load step after the last stability cycle.
$t_{\text{stab,1st}} @ 480 \text{ mA}$	Stabilization time at the high load step after the first stability cycle.
$t_{\text{stab,120th}} @ 480 \text{ mA}$	Stabilization time at the high load step after the last stability cycle.

Experimental conditions: unpurified 6 M KOH electrolyte at 50 °C; flow rate: 100 mL·min⁻¹.

Values shown in **Tables S1** and **S2** indicate the standard deviation derived from three replicate measurements.



Scheme S1. Recommended workflow for conducting electrochemical measurements to evaluate electrocatalytic stability in lab-scale water electrolyzers under fluctuating current conditions.



Scheme S2. Recommended workflow for conducting electrochemical measurements to evaluate electrocatalytic stability in lab-scale water electrolyzers under simulated shutdown conditions.

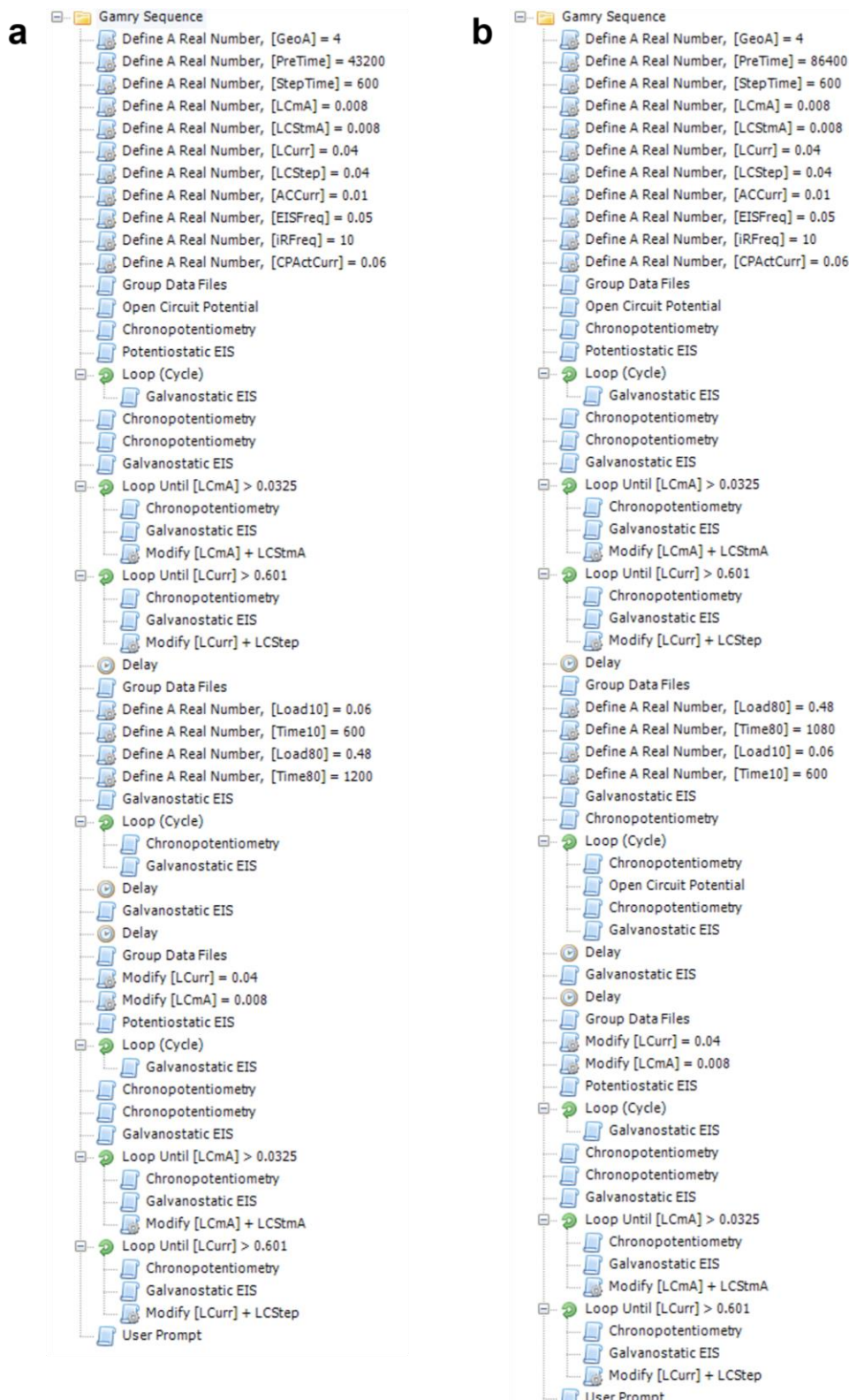


Figure S29. Experimental sequences constructed in the Gamry Sequence Wizard displaying an automated sequence of measurements to evaluate electrocatalytic stability in lab-scale water electrolyzers under (a) fluctuating current and (b) simulated shutdown conditions.

References

- (1) Márquez, R. A.; Kawashima, K.; Son, Y. J.; Castelino, G.; Miller, N.; Smith, L. A.; Chukwuneke, C. E.; Mullins, C. B. Getting the Basics Right: Preparing Alkaline Electrolytes for Electrochemical Applications. *ACS Energy Lett.* **2023**, *8* (2), 1141–1146. <https://doi.org/10.1021/acsenergylett.2c02847>.
- (2) Hoang, T. T. H.; Gewirth, A. A. High Activity Oxygen Evolution Reaction Catalysts from Additive-Controlled Electrodeposited Ni and NiFe Films. *ACS Catal.* **2016**, *6* (2), 1159–1164. <https://doi.org/10.1021/acscatal.5b02365>.
- (3) Yoon, Y.; Yan, B.; Surendranath, Y. Suppressing Ion Transfer Enables Versatile Measurements of Electrochemical Surface Area for Intrinsic Activity Comparisons. *J. Am. Chem. Soc.* **2018**, *140* (7), 2397–2400. <https://doi.org/10.1021/jacs.7b10966>.
- (4) Morales, D. M.; Risch, M. Seven Steps to Reliable Cyclic Voltammetry Measurements for the Determination of Double Layer Capacitance. *J. Phys. Energy* **2021**, *3* (3), 034013. <https://doi.org/10.1088/2515-7655/abee33>.
- (5) Márquez-Montes, R. A.; Collins-Martínez, V. H.; Pérez-Reyes, I.; Chávez-Flores, D.; Graeve, O. A.; Ramos-Sánchez, V. H. Electrochemical Engineering Assessment of a Novel 3D-Printed Filter-Press Electrochemical Reactor for Multipurpose Laboratory Applications. *ACS Sustain. Chem. Eng.* **2020**, *8* (9), 3896–3905. <https://doi.org/10.1021/acssuschemeng.9b07368>.
- (6) Son, Y. J.; Marquez, R. A.; Kawashima, K.; Smith, L. A.; Chukwuneke, C. E.; Babauta, J.; Mullins, C. B. Navigating iR Compensation: Practical Considerations for Accurate Study of Oxygen Evolution Catalytic Electrodes. *ACS Energy Lett.* **2023**, *8* (10), 4323–4329. <https://doi.org/10.1021/acsenergylett.3c01658>.
- (7) de Groot, M. T. Alkaline Water Electrolysis: With or without Iron in the Electrolyte? *Curr. Opin. Chem. Eng.* **2023**, *42*, 100981. <https://doi.org/10.1016/j.coche.2023.100981>.
- (8) Demnitz, M.; Lamas, Y. M.; Garcia Barros, R. L.; de Leeuw den Bouter, A.; van der Schaaf, J.; Theodorus de Groot, M. Effect of Iron Addition to the Electrolyte on Alkaline Water Electrolysis Performance. *iScience* **2023**, 108695. <https://doi.org/10.1016/j.isci.2023.108695>.
- (9) Bernt, M.; Gasteiger, H. A. Influence of Ionomer Content in IrO₂/TiO₂ Electrodes on PEM Water Electrolyzer Performance. *J. Electrochem. Soc.* **2016**, *163* (11), F3179. <https://doi.org/10.1149/2.0231611jes>.
- (10) Bender, G.; Carmo, M.; Smolinka, T.; Gago, A.; Danilovic, N.; Mueller, M.; Ganci, F.; Fallisch, A.; Lettenmeier, P.; Friedrich, K. A.; Ayers, K.; Pivovar, B.; Mergel, J.; Stolten, D. Initial Approaches in Benchmarking and Round Robin Testing for Proton Exchange Membrane Water Electrolyzers. *Int. J. Hydrogen Energy* **2019**, *44* (18), 9174–9187. <https://doi.org/10.1016/j.ijhydene.2019.02.074>.
- (11) Bernt, M.; Siebel, A.; Gasteiger, H. A. Analysis of Voltage Losses in PEM Water Electrolyzers with Low Platinum Group Metal Loadings. *J. Electrochem. Soc.* **2018**, *165* (5), F305–F314. <https://doi.org/10.1149/2.0641805jes>.
- (12) Ju, W.; Heinz, M. V. F.; Pusterla, L.; Hofer, M.; Fumey, B.; Castiglioni, R.; Pagani, M.; Battaglia, C.; Vogt, U. F. Lab-Scale Alkaline Water Electrolyzer for Bridging Material Fundamentals with Realistic Operation. *ACS Sustainable Chem. Eng.* **2018**, *6* (4), 4829–4837. <https://doi.org/10.1021/acssuschemeng.7b04173>.
- (13) Möckl, M.; Ernst, M. F.; Kornherr, M.; Allebrod, F.; Bernt, M.; Byrknes, J.; Eickes, C.; Gebauer, C.; Moskovtseva, A.; Gasteiger, H. A. Durability Testing of Low-Iridium PEM Water Electrolysis Membrane Electrode Assemblies. *J. Electrochem. Soc.* **2022**, *169* (6), 064505. <https://doi.org/10.1149/1945-7111/ac6d14>.
- (14) Kawashima, K.; Márquez-Montes, R. A.; Li, H.; Shin, K.; Cao, C. L.; Vo, K. M.; Son, Y. J.; Wygant, B. R.; Chunangad, A.; Youn, D. H.; Henkelman, G.; Ramos-Sánchez, V. H.; Mullins, C. B.

Electrochemical Behavior of a Ni₃N OER Precatalyst in Fe-Purified Alkaline Media: The Impact of Self-Oxidation and Fe Incorporation. *Mater. Adv.* **2021**, *2*, 2299–2309. <https://doi.org/10.1039/D1MA00130B>.

- (15) Anantharaj, S.; Kundu, S.; Noda, S. "The Fe Effect": A Review Unveiling the Critical Roles of Fe in Enhancing OER Activity of Ni and Co Based Catalysts. *Nano Energy* **2021**, *80*, 105514. <https://doi.org/10.1016/j.nanoen.2020.105514>.
- (16) Trotochaud, L.; Young, S. L.; Ranney, J. K.; Boettcher, S. W. Nickel–Iron Oxyhydroxide Oxygen-Evolution Electrocatalysts: The Role of Intentional and Incidental Iron Incorporation. *J. Am. Chem. Soc.* **2014**, *136* (18), 6744–6753. <https://doi.org/10.1021/ja502379c>.
- (17) Ehlers, J. C.; Feidenhans'l, A. A.; Therkildsen, K. T.; Larrazábal, G. O. Affordable Green Hydrogen from Alkaline Water Electrolysis: Key Research Needs from an Industrial Perspective. *ACS Energy Lett.* **2023**, 1502–1509. <https://doi.org/10.1021/acsenergylett.2c02897>.
- (18) Son, Y. J.; Kim, S.; Leung, V.; Kawashima, K.; Noh, J.; Kim, K.; Marquez, R. A.; Carrasco-Jaim, O. A.; Smith, L. A.; Celio, H.; Milliron, D. J.; Korgel, B. A.; Mullins, C. B. Effects of Electrochemical Conditioning on Nickel-Based Oxygen Evolution Electrocatalysts. *ACS Catal.* **2022**, *12* (16), 10384–10399. <https://doi.org/10.1021/acscatal.2c01001>.
- (19) Lira Garcia Barros, R.; Kraakman, J. T.; Sebregts, C.; van der Schaaf, J.; de Groot, M. T. Impact of an Electrode-Diaphragm Gap on Diffusive Hydrogen Crossover in Alkaline Water Electrolysis. *Int. J. Hydrogen Energy* **2023**. <https://doi.org/10.1016/j.ijhydene.2023.09.280>.
- (20) Iglesias van Montfort, H.-P.; Subramanian, S.; Irtem, E.; Sassenburg, M.; Li, M.; Kok, J.; Middelkoop, J.; Burdyny, T. An Advanced Guide to Assembly and Operation of CO₂ Electrolyzers. *ACS Energy Lett.* **2023**, 4156–4161. <https://doi.org/10.1021/acsenergylett.3c01561>.
- (21) Klaus, S.; Cai, Y.; Louie, M. W.; Trotochaud, L.; Bell, A. T. Effects of Fe Electrolyte Impurities on Ni(OH)₂/NiOOH Structure and Oxygen Evolution Activity. *J. Phys. Chem. C* **2015**, *119* (13), 7243–7254. <https://doi.org/10.1021/acs.jpcc.5b00105>.
- (22) Chukwuneke, C. E.; Kawashima, K.; Li, H.; Marquez, R. A.; Son, Y. J.; Smith, L. A.; Celio, H.; Henkelman, G.; Mullins, C. B. Electrochemically Engineered Domain: Nickel–Hydroxide/Nickel Nitride Composite for Alkaline HER Electrocatalysis. *J. Mater. Chem. A* **2023**. <https://doi.org/10.1039/D3TA06408E>.
- (23) Kim, Y.; Jung, S.-M.; Kim, K.-S.; Kim, H.-Y.; Kwon, J.; Lee, J.; Cho, H.-S.; Kim, Y.-T. Cathodic Protection System against a Reverse-Current after Shut-Down in Zero-Gap Alkaline Water Electrolysis. *JACS Au* **2022**, *2* (11), 2491–2500. <https://doi.org/10.1021/jacsau.2c00314>.
- (24) Huang, L.-F.; Hutchison, M. J.; Santucci, R. J.; Scully, J. R.; Rondinelli, J. M. Improved Electrochemical Phase Diagrams from Theory and Experiment: The Ni–Water System and Its Complex Compounds. *J. Phys. Chem. C* **2017**, *121* (18), 9782–9789. <https://doi.org/10.1021/acs.jpcc.7b02771>.